

Moments of nucleon generalized parton distributions from lattice QCD



C. Alexandrou ^(a,b), J. Carbonell ^(c), M. Constantinou ^(a), P. A. Harraud ^(c),
 P. Guichon ^(d), K. Jansen ^e, C. Kallidonis ^(a), T. Korzec ^(a,f), M. Papinutto ^(c)

^(a) *Department of Physics, University of Cyprus, P.O. Box 20537, 1678 Nicosia, Cyprus*

^(b) *Computation-based Science and Technology Research Center,
 Cyprus Institute, 20 Kavafi Str., 2121 Nicosia, Cyprus*

^(c) *Laboratoire de Physique Subatomique et Cosmologie,
 UJF/CNRS/IN2P3, 53 avenue des Martyrs, 38026 Grenoble, France*

^(d) *CEA-Saclay, IRFU/Service de Physique Nucléaire, 91191 Gif-sur-Yvette, France*

^(e) *NIC, DESY, Platanenallee 6, D-15738 Zeuthen, Germany*

^(f) *Institut für Physik Humboldt Universität zu Berlin, Newtonstrasse 15, 12489 Berlin, Germany*

We present results on the lower moments of the nucleon generalized parton distributions within lattice QCD using two dynamical flavors of degenerate twisted mass fermions. Our simulations are performed on lattices with three different values of the lattice spacings, namely $a = 0.089$ fm, $a = 0.070$ fm and $a = 0.056$ fm, allowing the investigation of cut-off effects. The volume dependence is examined using simulations on two lattices of spatial length $L = 2.1$ fm and $L = 2.8$ fm. The simulations span pion masses in the range of \overline{MS} 260–470 MeV. Our results are renormalized non-perturbatively and the values are given in the \overline{MS} scheme at a scale $\mu = 2$ GeV. They are chirally extrapolated to the physical point in order to compare with experiment. The consequences of these results on the spin carried by the quarks in the nucleon are investigated.

PACS numbers: 11.15.Ha, 12.38.Gc, 12.38.Aw, 12.38.-t, 14.70.Dj

I. INTRODUCTION

Lattice QCD calculations of observables, related to the structure of baryons, are now carried out using simulations of the theory with parameters that are close enough to their physical values that a connection of lattice results to experiment is facilitated. This is due to the fact that systematic uncertainties caused by a finite volume, a finite lattice cut-off and unphysically high pion masses are becoming better controlled. Nowadays, a number of major collaborations are producing results on nucleon form factors and the first moments of structure functions close to the physical regime both in terms of pion mass and with respect to the continuum limit [1–6].

The Generalized Parton Distributions (GPDs) encode important information related to baryon structure [7–9]. They occur in several physical processes such as Deeply Virtual Compton Scattering and Deeply Virtual Meson Production. Their forward limit coincides with the usual parton distributions and their first moments are related to the nucleon elastic form factors. Moreover a combination of their second moments, known as Ji’s sum rule [10], allows to determine the contribution of a specific parton to the nucleon angular momentum. In the context of the “proton spin puzzle” this has triggered an intense experimental activity [11–15].

The GPDs can be accessed in high energy processes where QCD factorization applies, in which case the amplitude is the convolution of a hard perturbative kernel with the GPDs, as illustrated in Fig. 1. Generically the GPDs are defined as matrix elements of bi-local operators separated by a light-like interval. Due to the Wick rotation such matrix elements cannot be computed directly on the Euclidean lattice. Instead one considers their Mellin moments, which in principle, carry the same information.

If $|p'\rangle$ and $|p\rangle$ are one-particle states, the twist-2 GPDs, which are studied in this paper, are defined by the matrix element [16]:

$$F_{\Gamma}(x, \xi, q^2) = \frac{1}{2} \int \frac{d\lambda}{2\pi} e^{ix\lambda} \langle p' | \bar{\psi}(-\lambda n/2) \Gamma \mathcal{P} e^{ig \int_{-\lambda/2}^{\lambda/2} d\alpha n \cdot A(n\alpha)} \psi(\lambda n/2) | p \rangle, \quad (1)$$

where $q = p' - p$, $\xi = -n \cdot q/2$, x is the momentum fraction, and n is a light-like vector collinear to $P = (p + p')/2$ and such that $P \cdot n = 1$. The gauge link $\mathcal{P} \exp(\dots)$ is necessary for gauge invariance. In model calculations it is often set to one, which amounts to working with QCD in the light-like gauge $A \cdot n = 0$, but on the lattice such a gauge fixing is not necessary.

In this work we shall consider only the GPDs corresponding to a Dirac structure Γ which conserves the quark chirality, that is $\Gamma = \not{n}$ and $\Gamma = \not{n}\gamma_5$. The associated matrix elements may be parametrized in the following way:

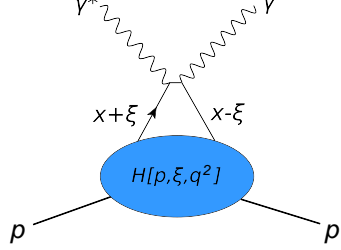


FIG. 1: “Handbag” diagram.

$$F_{\not{n}}(x, \xi, q^2) = \frac{1}{2} \bar{u}_N(p') \left[\not{n} H(x, \xi, q^2) + i \frac{n_\mu q_\nu \sigma^{\mu\nu}}{2m_N} E(x, \xi, q^2) \right] u_N(p) \quad (2)$$

$$F_{\not{n}\gamma_5}(x, \xi, q^2) = \frac{1}{2} \bar{u}_N(p') \left[\not{n}\gamma_5 \tilde{H}(x, \xi, q^2) + \frac{n \cdot q \gamma_5}{2m_N} \tilde{E}(x, \xi, q^2) \right] u_N(p). \quad (3)$$

where u_N is a nucleon spinor and $H, E, \tilde{H}, \tilde{E}$ are the twist-2 chirality even GPDs. In the forward limit for which $\xi = 0$ and $q^2 = 0$ they reduce to the ordinary parton distributions, namely the longitudinal momentum $q(x)$ and the helicity $\Delta q(x)$ distributions are given by:

$$q(x) = H(x, 0, 0), \quad \text{and} \quad \Delta q(x) = \tilde{H}(x, 0, 0). \quad (4)$$

The first few Mellin moments of these parton distributions are of particular interest

$$\langle x^{n-1} \rangle_q = \int_{-1}^1 x^{n-1} q(x) dx \quad (5)$$

$$\langle x^{n-1} \rangle_{\Delta q} = \int_{-1}^1 x^{n-1} \Delta q(x) dx. \quad (6)$$

Since as already mentioned, matrix elements of the light-cone operator as defined in Eq.(1) cannot be extracted from correlators in euclidean lattice QCD, the usual method is to proceed with an operator product expansion of this operator that leads to a tower of local operators given by:

$$\mathcal{O}_V^{\mu_1 \dots \mu_n} = \bar{\psi} \gamma^{\{\mu_1} i \overleftrightarrow{D}^{\mu_2} \dots i \overleftrightarrow{D}^{\mu_n\} \psi \quad (7)$$

$$\mathcal{O}_A^{\mu_1 \dots \mu_n} = \bar{\psi} \gamma^{\{\mu_1} i \overleftrightarrow{D}^{\mu_2} \dots i \overleftrightarrow{D}^{\mu_n\} \gamma_5 \psi. \quad (8)$$

The curly brackets represent a symmetrization over indices and subtraction of traces. The computation of the matrix elements of these operators on the Euclidean lattice can be done with standard techniques. The case $n = 1$ amounts to calculating the elastic form factors of the vector and axial-vector currents and the results are reported in Ref. [4, 17]. In this work we concentrate on the $n = 2$ moments, i.e. matrix elements of operators with a single derivative. The matrix elements of these operators are parametrized in terms of the generalized form factors (GFFs) $A_{20}(q^2)$, $B_{20}(q^2)$, $C_{20}(q^2)$ and $\tilde{A}_{20}(q^2)$, $\tilde{B}_{20}(q^2)$, according to

$$\langle N(p', s') | \mathcal{O}_{\not{n}}^{\mu\nu} | N(p, s) \rangle = \bar{u}_N(p', s') \left[A_{20}(q^2) \gamma^{\{\mu} P^{\nu\}} + B_{20}(q^2) \frac{i \sigma^{\{\mu\alpha} q_\alpha P^{\nu\}}}{2m} + C_{20}(q^2) \frac{1}{m} q^{\{\mu} q^{\nu\}} \right] u_N(p, s), \quad (9)$$

$$\langle N(p', s') | \mathcal{O}_{\not{n}\gamma_5}^{\mu\nu} | N(p, s) \rangle = \bar{u}_N(p', s') \left[\tilde{A}_{20}(q^2) \gamma^{\{\mu} P^{\nu\}} \gamma_5 + \tilde{B}_{20}(q^2) \frac{q^{\{\mu} P^{\nu\}}}{2m} \gamma_5 \right] u_N(p, s).$$

Note that the GFFs depend only on the squared momentum transfer $q^2 = (p' - p)^2$ which implies that the moments of the GPDs are polynomial in ξ . In the forward limit we have $A_{20}(0) = \langle x \rangle_q$ and $\tilde{A}_{20}(0) = \langle x \rangle_{\Delta q}$, which are respectively the first moment of the unpolarized and polarized quark distributions. Knowing the GFFs one can evaluate the quark contribution to the nucleon spin using Ji's sum rule: $J^q = \frac{1}{2}[A_{20}^q(0) + B_{20}^q(0)]$. Moreover, using the measured or calculated value of the quark helicity $\Delta\Sigma^q = g_A^q$ the decomposition $J^q = \frac{1}{2}\Delta\Sigma^q + L^q$ allows to study the role of the quark orbital angular momentum L^q .

II. LATTICE EVALUATION

Twisted mass fermions [18] provide an attractive formulation of lattice QCD that allows for automatic $\mathcal{O}(a)$ improvement, infrared regularization of small eigenvalues and fast dynamical simulations [19]. For the calculation of the moments of GPDs, which is the main focus of this work, the automatic $\mathcal{O}(a)$ improvement is particularly relevant since it is achieved by tuning only one parameter in the action, requiring no further improvements on the operator level.

The action for two degenerate flavors of quarks in twisted mass QCD is given by

$$S = S_g + \sum_x \bar{\chi}(x) [D_W + m_{\text{crit}} + i\gamma_5 \tau^3 \mu] \chi(x), \quad (10)$$

where D_W is the Wilson Dirac operator and we use the tree-level Symanzik improved gauge action S_g [20]. The quark fields χ are in the so-called ‘‘twisted basis’’ obtained from the ‘‘physical basis’’ at maximal twist by a simple transformation:

$$\psi = \frac{1}{\sqrt{2}}[\mathbf{1} + i\tau^3 \gamma_5] \chi \quad \text{and} \quad \bar{\psi} = \bar{\chi} \frac{1}{\sqrt{2}}[\mathbf{1} + i\tau^3 \gamma_5]. \quad (11)$$

We note that, in the continuum, this action is equivalent to the standard QCD action. As we pointed out, a crucial advantage is the fact that by tuning a single parameter, namely the bare untwisted quark mass to its critical value m_{crit} , a wide class of physical observables are automatically $\mathcal{O}(a)$ improved [18, 19, 21]. A disadvantage is the explicit flavor symmetry breaking. In a recent paper we have checked that this breaking is small for the baryon observables under consideration in this work and for the lattice spacings that we use [22–26]. To extract the GFFs without needing to evaluate the disconnected contributions we evaluate the nucleon matrix elements corresponding to the operators defined by

$$\mathcal{O}_{V_a}^{\mu_1 \dots \mu_n} = \bar{\psi} \gamma^{\{\mu_1} iD^{\mu_2} \dots iD^{\mu_n\}} \frac{\tau^a}{2} \psi, \quad \mathcal{O}_{A_a}^{\mu_1 \dots \mu_n} = \bar{\psi} \gamma^5 \gamma^{\{\mu_1} iD^{\mu_2} \dots iD^{\mu_n\}} \frac{\tau^a}{2} \psi, \quad (12)$$

where from now on we use the notation $\mathcal{O}_{V_a}^{\mu_1 \dots \mu_n}$ and $\mathcal{O}_{A_a}^{\mu_1 \dots \mu_n}$ to denote the vector and axial-vector operators with flavor index a . These matrix elements receive contributions only from the connected diagram for $a = 1, 2$ and up to $\mathcal{O}(a^2)$ for $a = 3$ [27]. In particular, we consider the isovector combination with $a = 3$ for which the form of the operators remain the same in the physical and twisted basis. In order to find the spin carried by each quark in the nucleon we also analyse the isoscalar one-derivative vector and axial-vector operators. The latter receive contributions from disconnected fermion loops, which we neglect in this analysis. Simulations including a dynamical strange quark are also available within the twisted mass formulation. Comparison of the nucleon mass obtained with two dynamical flavors and the nucleon mass including a dynamical strange quark has shown negligible dependence on the dynamical strange quark [28]. We therefore expect the results on the nucleon moments to show little sensitivity on a dynamical strange quark. This is also confirmed by comparing our results to those where a dynamical strange quark is included.

In this work we consider simulations at three values of the coupling constant with lattice spacings 0.056 fm, 0.07 fm and to 0.089 fm determined from the nucleon mass. This enables us to obtain results in the continuum limit. We also examine finite size effects by comparing results on two lattices of spatial length $L = 2.1$ fm and $L = 2.8$ fm [29–31].

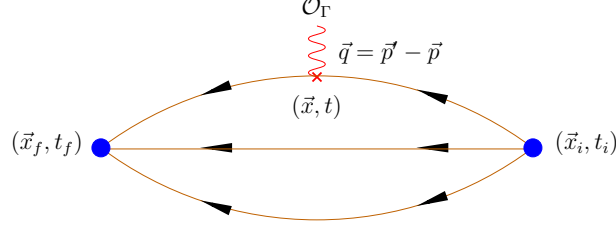


FIG. 2: Connected nucleon three-point function.

A. Correlation functions

The GFFs are extracted from dimensionless ratios of correlation functions. The two-point and three-point functions are defined by

$$G(\vec{q}, t_f - t_i) = \sum_{\vec{x}_f} e^{-i(\vec{x}_f - \vec{x}_i) \cdot \vec{q}} \Gamma_{\beta\alpha}^0 \langle J_\alpha(t_f, \vec{x}_f) \bar{J}_\beta(t_i, \vec{x}_i) \rangle \quad (13)$$

$$G^{\mu_1 \dots \mu_n}(\Gamma^\nu, \vec{q}, t - t_i) = \sum_{\vec{x}, \vec{x}_f} e^{i(\vec{x} - \vec{x}_i) \cdot \vec{q}} \Gamma_{\beta\alpha}^\nu \langle J_\alpha(t_f, \vec{x}_f) \mathcal{O}^{\mu_1 \dots \mu_n}(t, \vec{x}) \bar{J}_\beta(t_i, \vec{x}_i) \rangle, \quad (14)$$

where we consider kinematics for which the final momentum $p_f = 0$. We drop $t_f - t_i$ from the argument of the three-point function since it will be kept fixed in our approach. The projection matrices Γ^0 and Γ^k are given by:

$$\Gamma^0 = \frac{1}{4}(\mathbf{1} + \gamma_0), \quad \Gamma^k = i\Gamma^0 \gamma_5 \gamma_k \quad k = 1, 2, 3. \quad (15)$$

The proton interpolating field written in the twisted basis at maximal twist is given by

$$\tilde{J}(x) = \frac{1}{\sqrt{2}} [\mathbf{1} + i\gamma_5] \epsilon^{abc} \left[\tilde{u}^{a\top}(x) \mathcal{C} \gamma_5 \tilde{d}^b(x) \right] \tilde{u}^c(x). \quad (16)$$

where \mathcal{C} is the charge conjugation matrix. We use Gaussian smeared quark fields [32, 33] to increase the overlap with the proton state and decrease overlap with excited states. The smeared interpolating fields are given by:

$$\begin{aligned} q_{\text{smear}}^a(t, \vec{x}) &= \sum_{\vec{y}} F^{ab}(\vec{x}, \vec{y}; U(t)) q^b(t, \vec{y}), \\ F &= (\mathbf{1} + \alpha H)^n, \\ H(\vec{x}, \vec{y}; U(t)) &= \sum_{i=1}^3 [U_i(x) \delta_{x, y-i} + U_i^\dagger(x-i) \delta_{x, y+i}]. \end{aligned} \quad (17)$$

We also apply APE-smearing to the gauge fields U_μ entering the hopping matrix H . The parameters for the Gaussian smearing α and n are optimized using the nucleon mass as described in Ref. [6].

For correlators containing the isovector operators the disconnected diagrams are zero up to lattice artifacts, and can be safely neglected as we approach the continuum limit. The detailed investigation of volume and cut-off effects will be performed on isovector quantities, for which no contributions are neglected. They can be calculated by evaluating the connected diagram, shown schematically in Fig. 2. A standard approach to calculate the connected three-point function is using sequential inversions through the sink [34]. The creation operator is taken at a fixed position $\vec{x}_i = \vec{0}$ (source). The annihilation operator at a later time t_f (sink) carries momentum $\mathbf{p}' = 0$. The current couples to a quark at an intermediate time t and carries momentum \mathbf{q} . Translation invariance enforces $\mathbf{q} = -\mathbf{p}$ for our kinematics. At a fixed source-sink time separation we obtain results for all possible momentum transfers and insertion times as well as for any operator $\mathcal{O}^{\{\mu_1 \dots \mu_n\}}$, with one set of sequential inversions per choice of the sink. We perform separate inversions for each one of the four projection matrices Γ^μ given in Eq. (15).

Using the two- and three-point functions of Eqs. (13)-(15) and considering only one derivative operators we form the ratio

$$R^{\mu\nu}(\Gamma^\lambda, \vec{q}, t) = \frac{G^{\mu\nu}(\Gamma^\lambda \vec{q}, t)}{G(\vec{0}, t_f)} \sqrt{\frac{G(\vec{p}, t_f - t) G(\vec{0}, t) G(\vec{0}, t_f)}{G(\vec{0}, t_f - t) G(\vec{p}, t) G(\vec{p}, t_f)}}, \quad (18)$$

which is optimized because it does not contain potentially noisy two-point functions at large separations and because correlations between its different factors reduce the statistical noise. For sufficiently large separations $t_f - t$ and $t - t_i$ this ratio becomes time-independent (plateau region):

$$\lim_{t_f - t \rightarrow \infty} \lim_{t - t_i \rightarrow \infty} R^{\mu\nu}(\Gamma^\lambda, \vec{q}, t) = \Pi^{\mu\nu}(\Gamma^\lambda, \vec{q}). \quad (19)$$

From the plateau values of the renormalized asymptotic ratio $\Pi(\Gamma^\lambda, \vec{q})_R = Z\Pi(\Gamma^\lambda, \vec{q})$ the generalized form factors can be extracted. The equations relating $\Pi(\Gamma^\lambda, \vec{q})$ to the GFFs are given in Appendix A. All values of \vec{q}^2 , the four choices of Γ and the ten orientations μ, ν of the operator lead to an over-constrained system of equations which is solved in the least-squares sense via a singular value decomposition of the coefficient matrix. All quantities will be given in Euclidean space with $Q^2 = -q^2$ the Euclidean momentum transfer squared. The coefficients follow from the matrix-element decomposition given in Eq. (9) and may depend on the energy and mass of the nucleon as well as on the initial spatial momentum $\vec{p} = -\vec{q}$ (see Appendix A). It turns out that both the operators with $\mu = \nu$ and $\mu \neq \nu$ are necessary to obtain all three one-derivative vector form factors. Since those two classes of operators on a lattice renormalize differently from each other [35], renormalization has to be carried out already on the level of the ratios. Although the one-derivative axial form factors can be extracted using only correlators with $\mu \neq \nu$, we use all combinations of μ, ν in order to decrease the statistical error. In Fig. 3 we show representative plateaus for different momentum and indices μ and ν .

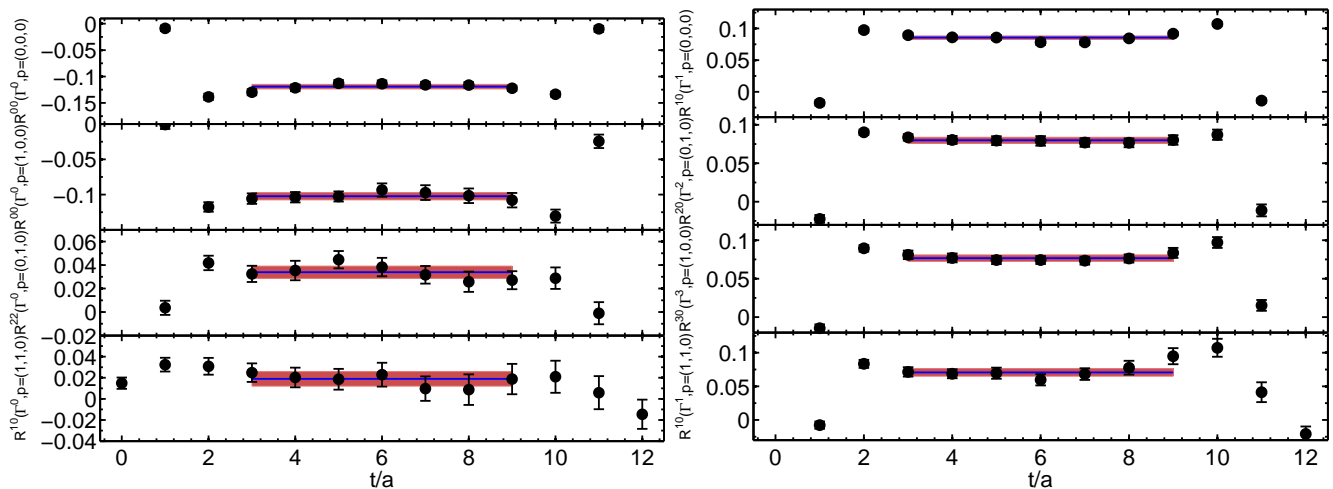


FIG. 3: Ratios for the one derivative vector (left) and axial vector (right) operator for a few exemplary choices of the momentum. The solid lines with the bands indicate the fitted plateau values with their jackknife errors. From top to bottom the momentum takes values $\vec{p} = (0, 0, 0); (0, 1, 0), (1, 0, 0)$ and $(1, 1, 0)$.

Since we use sequential inversions through the sink we need to fix the sink-source separation. The statistical errors on the three-point function are kept as small as possible by using the smallest value for the sink-source time separation that still ensures that the excited state contributions are sufficiently suppressed. We have tested different values of the sink-source time separation [17] and for the final results we use the following values which correspond to $t_f - t_i \sim 1$ fm

$$\beta = 3.9 : (t_f - t_i)/a=12, \quad \beta = 4.05 : (t_f - t_i)/a=16, \quad \beta = 4.20 : (t_f - t_i)/a=18.$$

B. Simulation details

The input parameters of the calculation, namely β , L/a and $a\mu$ are summarized in Table I. The lattice spacing a is determined from the nucleon mass, and the reader is referred to Ref. [6, 17] for more details. Here we present only the final values, which are

$$a_{\beta=3.9} = 0.089(1)(5), \quad a_{\beta=4.05} = 0.070(1)(4), \quad a_{\beta=4.2} = 0.056(2)(3),$$

where the first error is statistical and the second systematic. The pion mass values, spanning a range from 260 MeV to 470 MeV, are taken from Ref. [36]. At $m_\pi \approx 300$ MeV and $\beta=3.9$ we have simulations for lattices of spatial size

$L=2.1$ fm and $L=2.8$ fm allowing to investigate finite size effects. Finite lattice spacing effects are studied using three sets of results at $\beta=3.9$, $\beta=4.05$ and $\beta=4.2$ for the lowest and largest pion mass available in this work. These sets of gauge ensembles allow us to estimate all the systematic errors in order to produce reliable predictions for the nucleon one-derivative GFFs.

$\beta = 3.9, a = 0.089(1)(5)$ fm, $r_0/a = 5.22(2)$						
$24^3 \times 48, L = 2.1$ fm	$a\mu$		0.0040	0.0064	0.0085	0.010
	No. of confs		943	553	365	477
	m_π (GeV)		0.3032(16)	0.3770(9)	0.4319(12)	0.4675(12)
	$m_\pi L$		3.27	4.06	4.66	5.04
$32^3 \times 64, L = 2.8$ fm	$a\mu$	0.003	0.004			
	No. of confs	667	351			
	m_π (GeV)	0.2600(9)	0.2978(6)			
	$m_\pi L$	3.74	4.28			
$\beta = 4.05, a = 0.070(1)(4)$ fm, $r_0/a = 6.61(3)$						
$32^3 \times 64, L = 2.13$ fm	$a\mu$	0.0030	0.0060	0.0080		
	No. of confs	447	326	419		
	m_π (GeV)	0.2925(18)	0.4035(18)	0.4653(15)		
	$m_\pi L$	3.32	4.58	5.28		
$\beta = 4.2, a = 0.056(1)(4)$ fm $r_0/a = 8.31$						
$32^3 \times 64, L = 2.39$ fm	$a\mu$	0.0065				
	No. of confs	357				
	m_π (GeV)	0.4698(18)				
	$m_\pi L$	4.24				
$48^3 \times 96, L = 2.39$ fm	$a\mu$	0.002				
	No. of confs	245				
	m_π (GeV)	0.2622(11)				
	$m_\pi L$	3.55				

TABLE I: Input parameters ($\beta, L, a\mu$) of our lattice calculation and corresponding lattice spacing (a) and pion mass (m_π).

C. Renormalization

We determine the renormalization constants for the one-derivative operators non-perturbatively, in the RI'-MOM scheme [37]. We employ a momentum source [38] and perform a perturbative subtraction of $\mathcal{O}(a^2)$ terms [37, 39]. This subtracts the leading cut-off effects yielding only a very weak dependence of the renormalization factors on $(ap)^2$ for which the $(ap)^2 \rightarrow 0$ limit can be reliably taken. It was also shown with high accuracy that the quark mass dependence is negligible for the aforementioned operators. We find the values

$$\begin{aligned}
Z_V^{\mu=\nu} &= 0.970(26), 1.013(14), 1.097(6) \\
Z_V^{\mu\neq\nu} &= 1.061(29), 1.131(18), 1.122(10) \\
Z_A^{\mu\neq\nu} &= 1.076(1), 1.136(0), 1.165(10)
\end{aligned}
\tag{20}$$

at $\beta=3.9, 4.05$ and 4.2 respectively. These are the values that we use in this work to renormalize the lattice matrix element.

III. LATTICE RESULTS

In this section we present our results on the nucleon generalized form factors $A_{20}(Q^2), B_{20}(Q^2), C_{20}(Q^2)$ and $\tilde{A}_{20}(Q^2), \tilde{B}_{20}(Q^2)$. We examine their dependence on the lattice volume and spacing, as well as, on the pion mass. We

also compare with recent results from other collaborations. In particular, we discuss lattice artifacts for the results on the isovector combination for the renormalized nucleon matrix element of the one-derivative operators

$$\bar{u}\gamma_{\{\mu}\overleftrightarrow{D}_{\nu\}}u - \bar{d}\gamma_{\{\mu}\overleftrightarrow{D}_{\nu\}}d, \quad \bar{u}\gamma_5\gamma_{\{\mu}\overleftrightarrow{D}_{\nu\}}u - \bar{d}\gamma_5\gamma_{\{\mu}\overleftrightarrow{D}_{\nu\}}d$$

in the $\overline{\text{MS}}$ scheme at a scale $\mu = 2$ GeV.

In order to obtain some estimates on the spin content of the nucleon we also analyse the isoscalar parts of the spin-independent and helicity quark distributions, which however neglect the disconnected contributions.

The GFFs $A_{20}(Q^2 = 0)$ and $\tilde{A}_{20}(Q^2 = 0)$ are computed directly from the matrix elements, whereas $B_{20}(Q^2 = 0)$, $C_{20}(Q^2 = 0)$ and $\tilde{B}_{20}(Q^2 = 0)$ are obtained by linearly extrapolating the $Q^2 \neq 0$ data. C_{20} is consistent to zero within error bars for all momentum transfers.

A. Finite volume effects

In order to access volume effects we compare in Fig. 4 results on the moments $\langle x \rangle_{u-d}$ and $\langle x \rangle_{\Delta u-\Delta d}$ computed on different lattice sizes as a function of m_π^2 . As already mentioned, both these quantities are directly obtained at $Q^2 = 0$ and require no assumption on their Q^2 -dependence. Alongside our results we also show results using $N_F = 2$ clover fermions [40] (preliminary), $N_F = 2 + 1$ domain wall fermions (DWF) [41] and domain wall valence quarks on an $N_F = 2 + 1$ staggered sea (hybrid) [42].

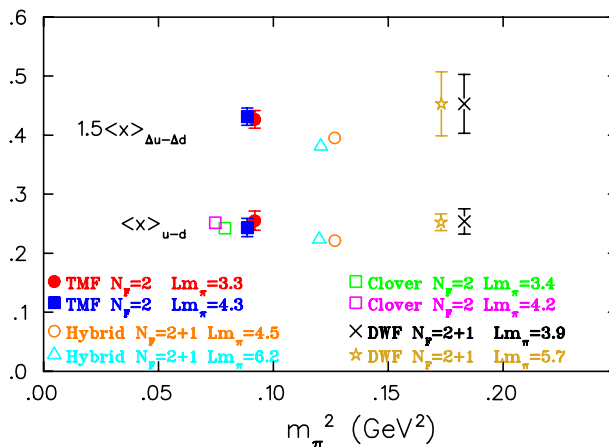


FIG. 4: $\langle x \rangle_{u-d}$ and $\frac{3}{2}\langle x \rangle_{\Delta u-\Delta d}$ using twisted mass fermions (this work), $N_F = 2$ clover fermions [40] (preliminary), hybrid [42] and DWF [41].

The results shown in Fig. 5 using twisted mass fermions correspond to a pion mass of about 300 MeV and are computed on lattices of spatial L with $Lm_\pi = 3.3$ and $Lm_\pi = 4.3$. As can be seen, results on these two lattices for both $\langle x \rangle_{u-d}$ and $\langle x \rangle_{\Delta u-\Delta d}$ are consistent. The LHPC using a hybrid approach and $m_\pi \sim 350$ MeV has very accurate results at two lattices with $Lm_\pi = 4.5$ and $Lm_\pi = 6.2$. No volume effects are seen for both vector and axial-vector first moments. The QCDSF collaboration has preliminary results for $\langle x \rangle_{u-d}$ using clover fermions for $m_\pi \sim 270$ MeV with $Lm_\pi = 3.4$ and $Lm_\pi = 4.2$, which are consistent. Finally the RBC-UKQCD results with domain wall fermions with $Lm_\pi = 3.9$ and $Lm_\pi = 5.7$ show no volume effects for both $\langle x \rangle_{u-d}$ and $\langle x \rangle_{\Delta u-\Delta d}$ [41]. The conclusion that we draw from this comparison is that finite volume effects on $\langle x \rangle_{u-d}$ and $\langle x \rangle_{\Delta u-\Delta d}$ are insignificant at our current statistical precision for lattices that satisfy $Lm_\pi > 3.3$.

In Figs. 5 we compare results on the GFFs $A_{20}(Q^2)$, $B_{20}(Q^2)$, $\tilde{A}_{20}(Q^2)$ and $\tilde{B}_{20}(Q^2)$ using twisted mass fermions for $m_\pi \sim 300$ MeV for our two spatial lattice sizes of $L = 2.1$ fm and $L = 2.8$ fm. The lines shown are linear fits to the Q^2 -dependence. As can be seen, for both $A_{20}(Q^2)$ and $\tilde{A}_{20}(Q^2)$ one can not ascertain any volume dependence. For $B_{20}(Q^2)$ and $\tilde{B}_{20}(Q^2)$ the statistical errors are larger and the linear fits show larger spread with the change in the spatial volume. However, given the large statistical uncertainties, it is difficult to quantify any volume dependence.

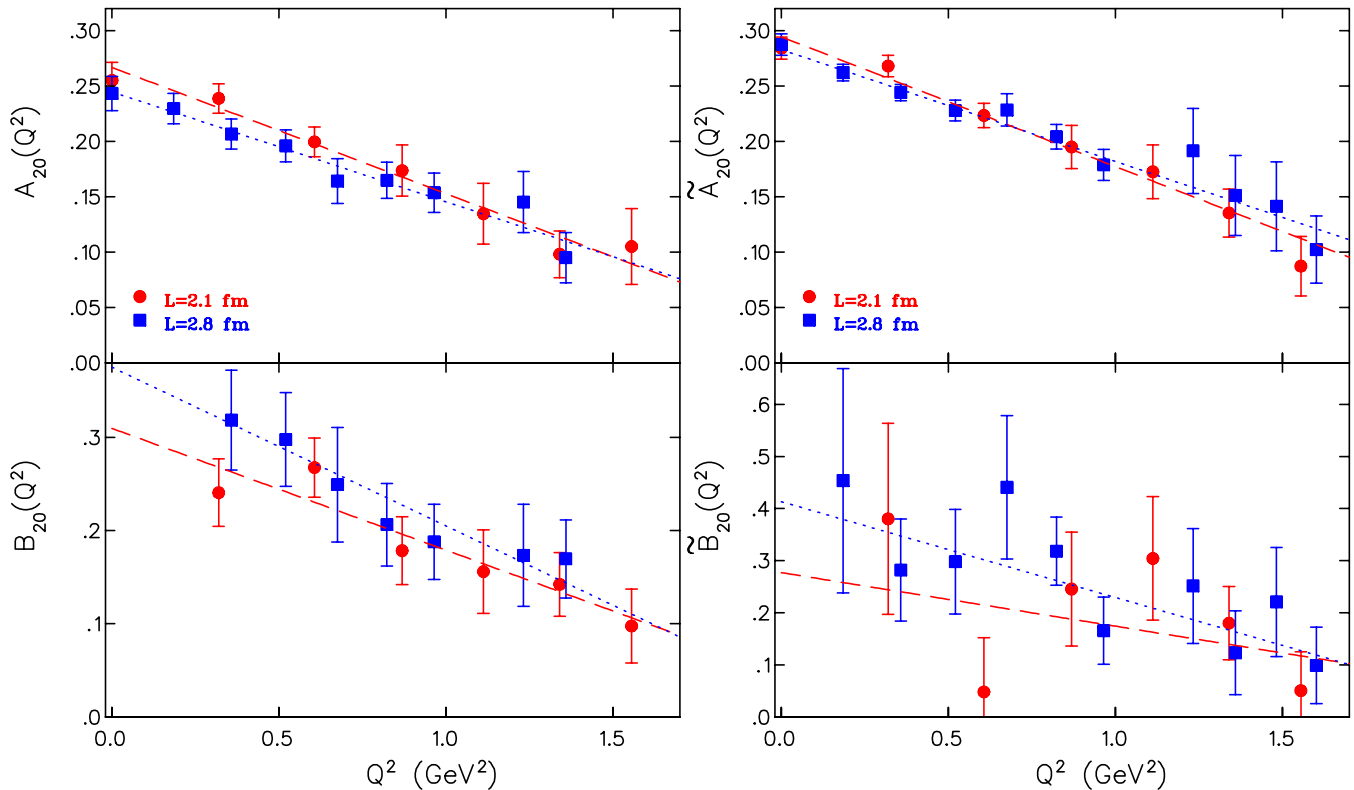


FIG. 5: Left panel: The isovector GFFs A_{20} and B_{20} for pion mass ~ 300 MeV for a lattice of spatial length $L = 2.1$ fm and $L = 2.8$ fm. Right panel: The axial-vector GFFs \tilde{A}_{20} and \tilde{B}_{20} for $L = 2.1$ fm and $L = 2.8$ fm.

B. Cut-off effects

In order to examine cut-off effects we compare in Fig. 6 our results obtained at the lowest and highest pion mass that we have considered in this work, namely $m_\pi \sim 260$ MeV and $m_\pi \sim 470$ MeV. We show results on the quantities $A_{20}(Q^2)$ and $\tilde{A}_{20}(Q^2)$ since these have smaller statistical errors than $B_{20}(Q^2)$ and $\tilde{B}_{20}(Q^2)$. For the heavier mass, where we have results at all three lattice spacings, there is no visible dependence on the lattice spacing especially at low Q^2 -values. For the lightest pion mass of $m_\pi = 260$ MeV we have results at the largest and smallest lattice spacings. The results are in good agreement although some deviations are seen at larger Q^2 -values. Thus, within our current statistical errors, one may conclude that no significant cut-off effects are observed.

C. Quark mass dependence

The mass dependence of A_{20} and \tilde{A}_{20} is shown in Fig. 7. Although the dependence on the mass is weak in the range of pion masses spanned, the tendency is for the values of the GFFs to decrease with decreasing pion mass. There is also a tendency for an increase in the slope for both A_{20} and \tilde{A}_{20} as the pion mass decreases.

D. Comparison with other discretization schemes

In order to compare lattice data using different discretization schemes one would have to first extrapolate to the continuum limit. However, given that the cut-off effects are small for lattice spacings of about 0.1 fm, lattice results for different values of a using a number of improved discretizations can be directly compared. In Fig. 8 we show results on the spin-independent and helicity moments using twisted mass fermions, in the hybrid approach obtained by LHPC [42], with $N_F = 2$ clover fermions by the QCDSF collaboration [40] (preliminary results) and with DWF by the RBC-UKQCD collaborations [41]. There is good agreement among lattice results. The very accurate results obtained using a hybrid action of domain wall valence and $N_F = 2 + 1$ staggered fermions [42] tend to be

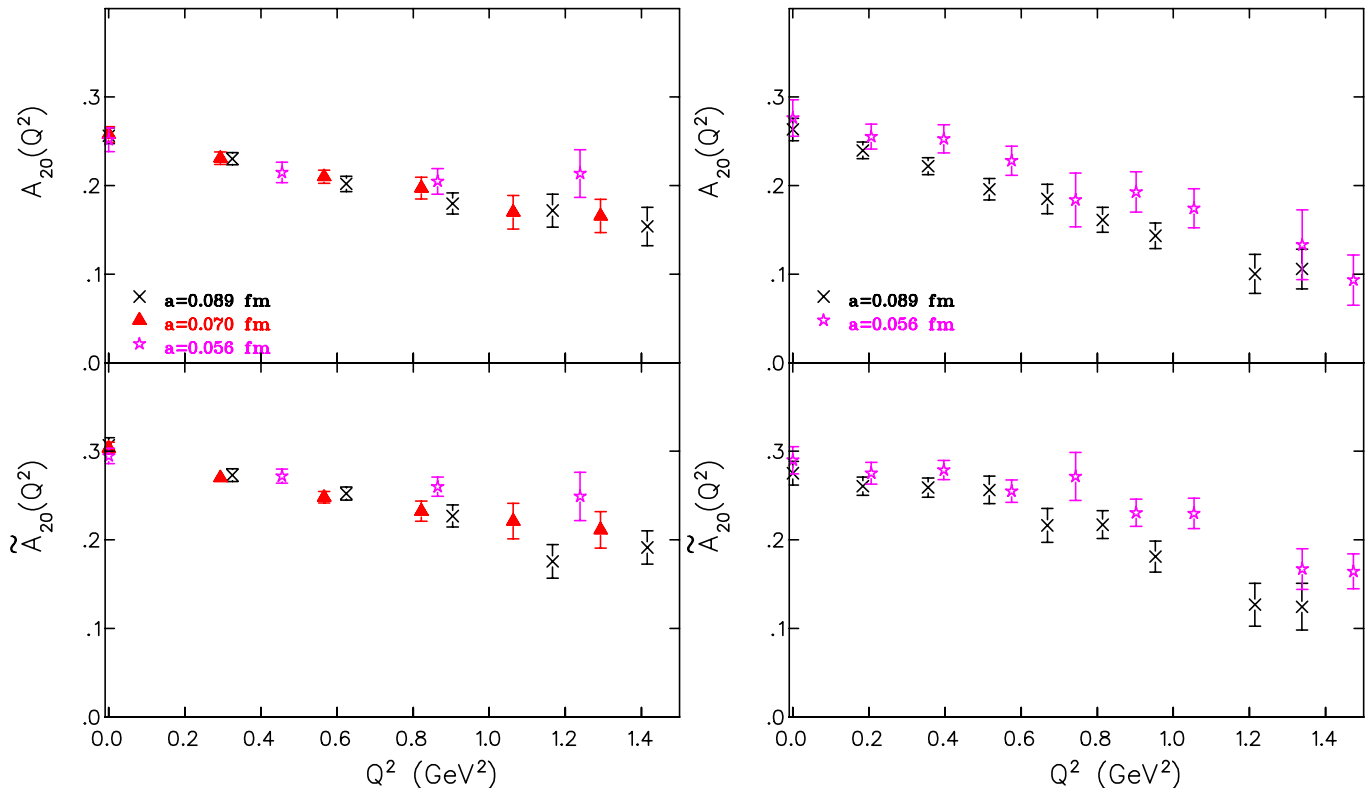


FIG. 6: Left panel: The GFFs A_{20} and \tilde{A}_{20} for our three lattice spacings at $m_\pi \sim 470$ MeV. Right panel: A_{20} and \tilde{A}_{20} for $a = 0.089$ fm and $a = 0.056$ fm at $m_\pi \sim 260$ MeV.

lower compared to the other data. One difference between them and the other results presented is that they are perturbatively renormalized. It was shown in Ref. [41] that perturbative renormalization can lead to lower values. The spread in the values of the lattice results is shown to be reduced by taking a renormalization free ratio leading to a better agreement among lattice data with $Lm_\pi > 4$ [43]. In particular, constructing a renormalization free ratio brought the hybrid data in agreement with our results using twisted mass fermions and those using clover fermions by QCDSF. Lattice values for $\langle x \rangle_{u-d} = A_{20}(Q^2 = 0)$ although compatible are higher from the phenomenological value $\langle x_{u-d} \rangle \sim 0.16$. The very recent preliminary result by QCDSF [40] at $m_\pi \sim 170$ MeV remains higher than experiment and highlights the need to understand such deviations. A similar conclusion holds for the helicity moment.

In Figs. 9 we compare our results for the GFFs with pion mass 300 MeV with those obtained using a hybrid action by LHPC and clover fermions by QCDSF and pion mass of 355 MeV and 350 MeV, respectively. The results show an overall agreement, with the data of LHPC somewhat lower than the other two sets. Once more the fact that both our results and those of QCDSF are renormalized non-perturbatively, while those of LHPC are renormalized perturbatively, might explain this difference. Moreover, in our determination of the renormalization constants, we have subtracted $\mathcal{O}(a^2)$ terms perturbatively to reduce lattice artifacts [37].

IV. CHIRAL PERTURBATION THEORY

In order to make a direct comparison with experiment we need to extrapolate to the physical point. We only perform chiral extrapolation of GFFs at $Q^2 = 0$. We first perform this extrapolation using our lattice results directly, since, as we have discussed in the previous section, cut-off effects are small. In the next section we will perform a continuum extrapolation and verify that indeed the values we find at the physical point are compatible.

Within heavy baryon chiral perturbation theory (HB χ PT) [49, 50] the expressions for the m_π -dependence of A_{20}

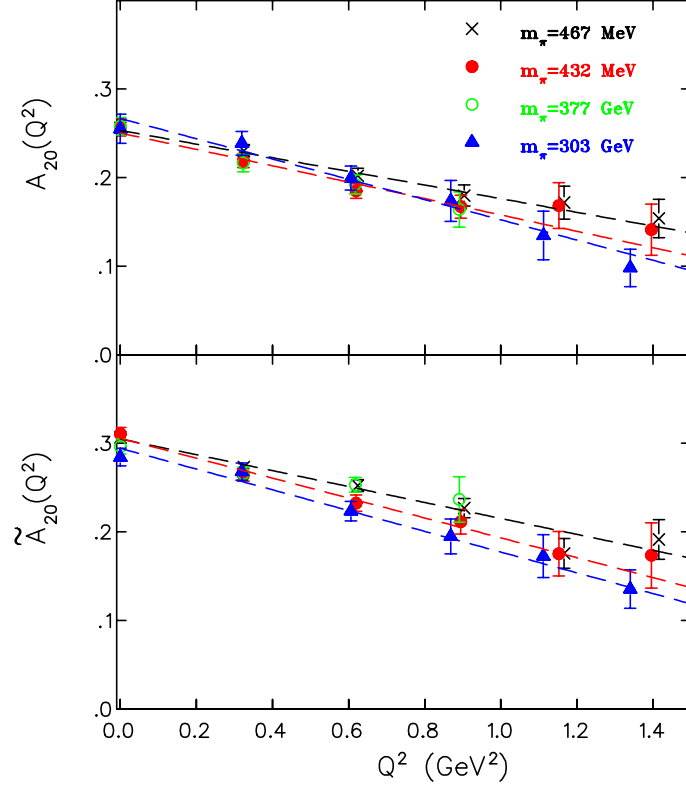


FIG. 7: Pion mass dependence of $A_{20}(Q^2)$ and $\tilde{A}_{20}(Q^2)$ computed at $\beta = 3.9$ and using a lattice size of $24^3 \times 48$.

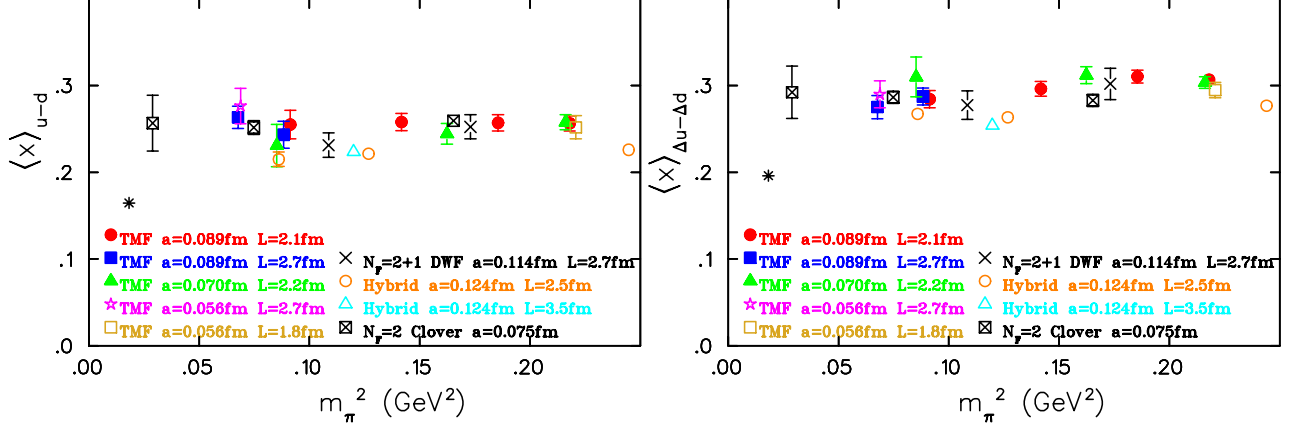


FIG. 8: Lattice data on $\langle x \rangle_{u-d}$ and $\langle x \rangle_{\Delta u - \Delta d}$ using: (i) $N_F = 2$ with $a = 0.089$ fm: filled red circles for $L = 2.1$ fm and filled blue squares for $L = 2.8$ fm, $a = 0.070$ fm: filled green triangles for $L = 2.2$ fm, $a = 0.056$ fm: purple star for $L = 2.7$ fm and open yellow square for $L = 1.8$ fm; (ii) $N_F = 2 + 1$ DWF [41] crosses for $a = 0.114$ fm and $L = 2.7$ fm; (iii) $N_F = 2 + 1$ using DWF for the valence quarks on staggered sea [42] with $a = 0.124$ fm: open orange circles for $L = 2.5$ fm and open cyan triangle for $L = 3.5$ fm; (iv) $N_F = 2$ clover with $a = 0.075$ fm [40] (Preliminary results). The physical point, shown by the asterisk, is from Ref. [44] for the unpolarized and from Ref. [45, 46] for the polarized first moment.

and \tilde{A}_{20} are given by:

$$\langle x \rangle_{u-d} = C \left[1 - \frac{3g_A^2 + 1}{(4\pi f_\pi)^2} m_\pi^2 \ln \frac{m_\pi^2}{\lambda^2} \right] + \frac{c_8(\lambda^2) m_\pi^2}{(4\pi f_\pi)^2}, \quad (21)$$

$$\langle x \rangle_{\Delta u - \Delta d} = \tilde{C} \left[1 - \frac{2g_A^2 + 1}{(4\pi f_\pi)^2} m_\pi^2 \ln \frac{m_\pi^2}{\lambda^2} \right] + \frac{\tilde{c}_8(\lambda^2) m_\pi^2}{(4\pi f_\pi)^2}, \quad (22)$$

where we take $\lambda^2 = 1 \text{ GeV}^2$. The best fit is shown in Fig. 10, where the width of the band is computed through

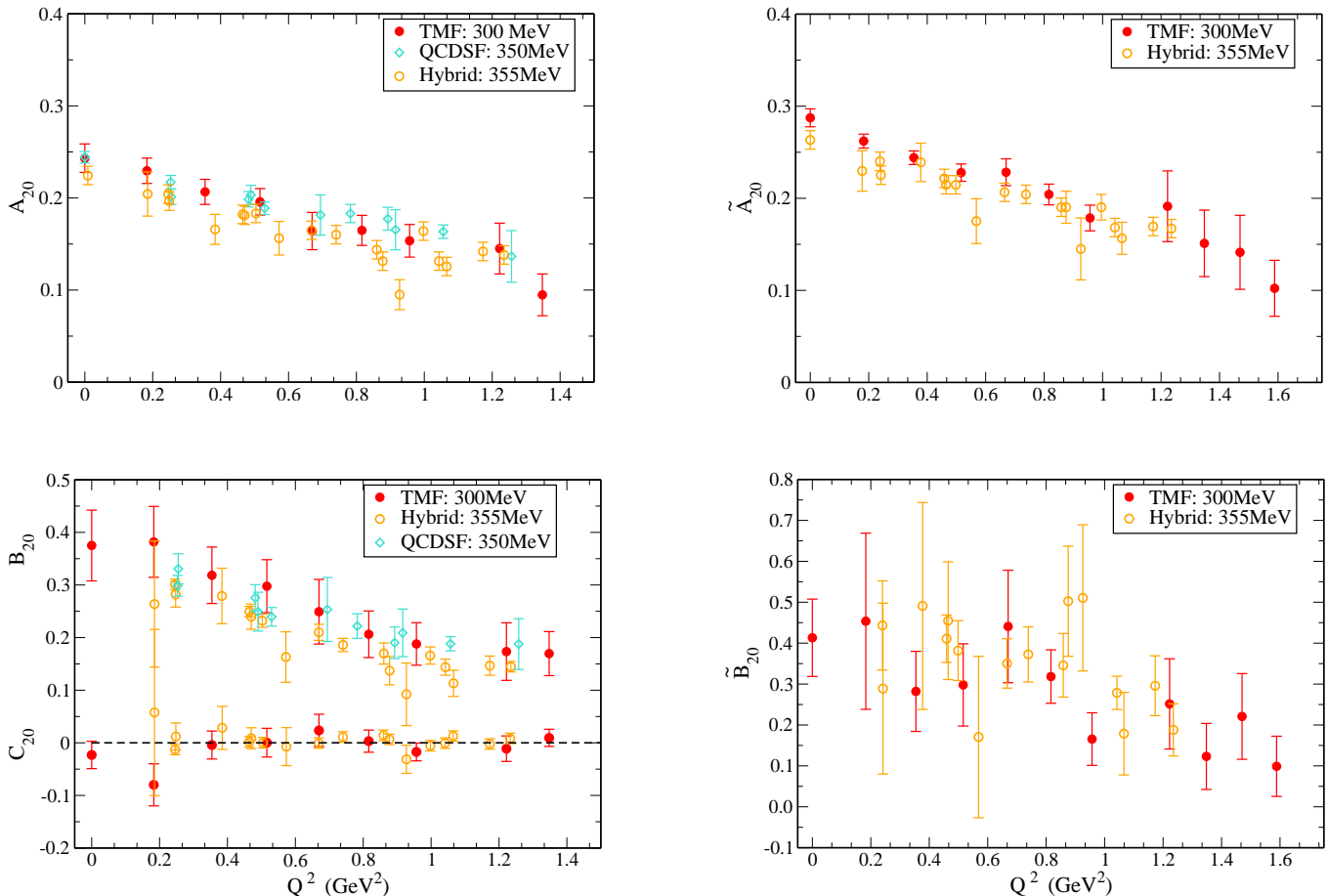


FIG. 9: Comparison of twisted mass results for $A_{20}(Q^2)$, $B_{20}(Q^2)$ and $C_{20}(Q^2)$ (left panel) and $\tilde{A}_{20}(Q^2)$ and $\tilde{B}_{20}(Q^2)$ (right panel) at pion mass 300 MeV with those obtained using a hybrid action at $m_\pi = 355$ MeV and $N_F = 2$ clover fermions at $m_\pi = 355$ MeV.

a super-jackknife analysis [42]. As can be seen, the fits yield a value higher than experiment for both observables. LHPC carried out a combined chiral fit using $\mathcal{O}(p^2)$ covariant baryon chiral perturbation theory (CB χ PT) [51] to A_{20} , B_{20} and C_{20} . The mass of the nucleon at the chiral limit is used as input to the fits. They obtained a value for A_{20} in agreement with experiment [42]. In order to compare with their analysis we also perform a combined fit to $A_{20}(0)$, $B_{20}(0)$ and $C_{20}(0)$ within CB χ PT [51]. The CB χ PT fits are shown by the bands in Fig. 11. As can be seen, they also provide a good description to the lattice data but, in the case of A_{20} , CB χ PT leads to an even higher value at the physical point. Therefore, the discrepancy between our lattice results and the experimental value is not resolved. In Appendix B we collect the formulae used for the chiral extrapolations. The actual renormalized lattice data are tabulated in the tables of Appendix C for the isovector GFFs.

V. CONTINUUM EXTRAPOLATION

In order to study the continuum extrapolation we use the simulations at our three lattice spacings at the smallest and largest pion mass. We first interpolate the GFFs at the three values of β to a given value of the pseudoscalar mass in units of r_0 . We take as reference pion masses the ones computed on the finest lattice and interpolate results at the other two β -values to these two reference masses.

As already mentioned, $\langle x \rangle_{u-d} = A_{20}(0)$ and $\langle x \rangle_{\Delta u - \Delta d} = \tilde{A}_{20}(0)$ are calculated directly at $Q^2 = 0$ requiring no fits. We therefore choose these quantities to examine their dependence on the lattice spacing since this choice avoids any systematic errors due to the extrapolation to $Q^2 = 0$, which would require the adaptation of an Ansatz for the Q^2 -dependence.

Having determined the values at a given reference pion mass, we perform a fit to these data using the form $y(a) = y(0) + c(a/r_0)^2$. The resulting fits are shown in Fig. 12. Setting $c = 0$ we obtained the constant line also

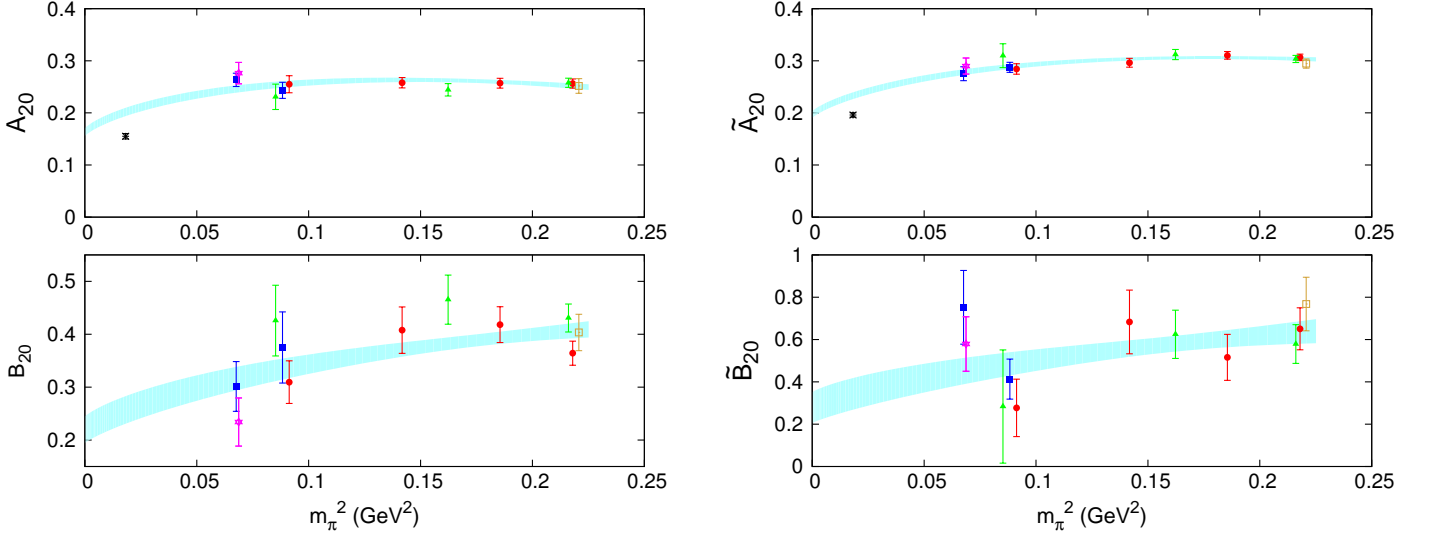


FIG. 10: Chiral extrapolation using HB χ PT for the isovector unpolarized and polarized first moment of the quark distributions. The physical point, shown by the asterisk, is from Ref. [44] for the unpolarized and from Ref. [45, 46] for the polarized first moment.

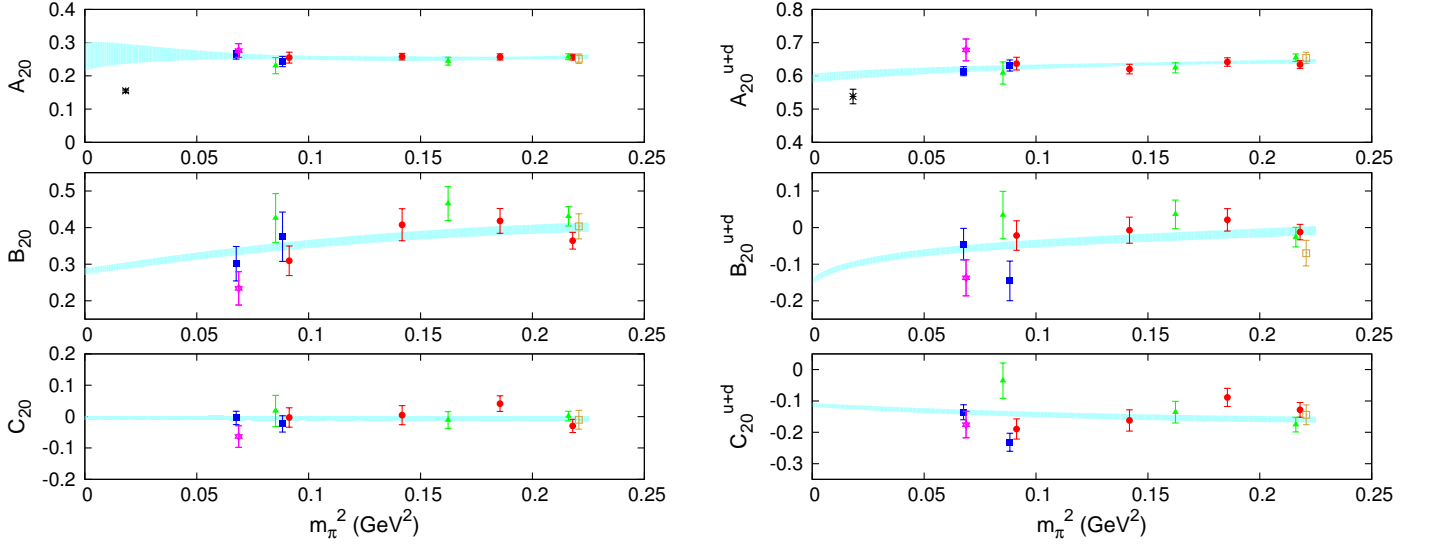


FIG. 11: Chiral extrapolation using CB χ PT for the isovector (left) and isoscalar (right) moments A_{20} , B_{20} and C_{20} . The physical point, shown by the asterisk, is from Ref. [44] for the isovector and from Refs. [47, 48] for the isoscalar.

shown in the figure. As can be seen, for both large and small pion masses allowing a non-zero slope yields a value in the continuum limit that is in agreement with that obtained using a constant fit. This analysis shows that finite a effects are small for both large and small pion masses and extrapolation to the continuum limit using a constant fit is acceptable. For the intermediate pion masses we therefore obtained the values in the continuum by fitting our data at $\beta = 3.9$ and $\beta = 4.05$ to a constant. For comparison we also perform a similar analysis for $B_{20}(0)$ which requires fitting the Q^2 -dependence. The qualitative behavior is similar to the one observed for $A_{20}(0)$ and $B_{20}(0)$.

Having results at the continuum limit we perform a chiral fit using HB χ PT. The resulting curves are shown in Fig. 13 and still produce a value at the physical point that is higher than the experimental value. In fact, the value obtained at the physical point for both vector and axial-vector moments is in agreement to the one extracted using the raw lattice data. This provides an *a posteriori* justification of using continuum chiral perturbation theory directly

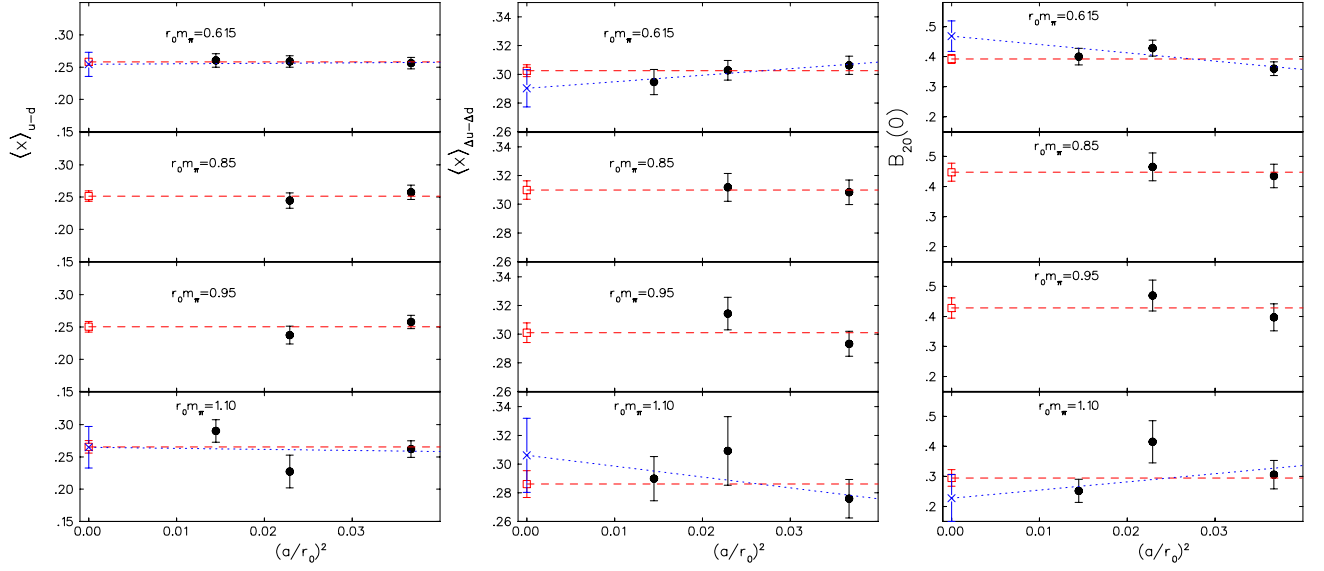


FIG. 12: $\langle x \rangle_{u-d}$, $\langle x \rangle_{\Delta u - \Delta d}$ and $B_{20}(0)$ as a function of $(a/r_0)^2$. The red line is the result of fitting to a constant; the blue one is a linear fit.

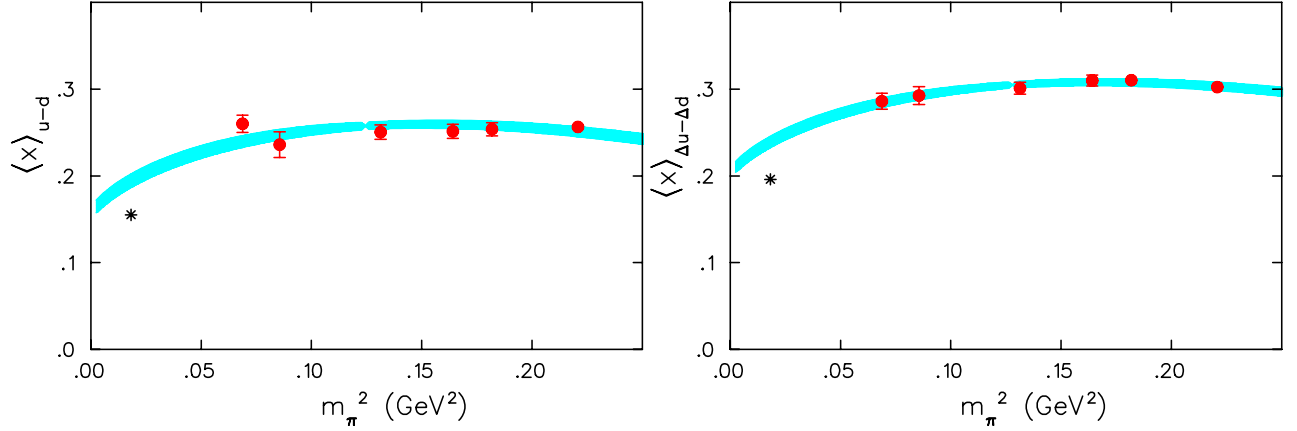


FIG. 13: $\langle x \rangle_{u-d}$ (left) and $\langle x \rangle_{\Delta u - \Delta d}$ (right) extrapolated to $a = 0$ as a function of m_π . The blue band is the chiral fit using HB χ PT. The physical point, shown by the asterisk, is from Ref. [44] for the unpolarized and from Refs. [45, 46] for the polarized first moment.

on the lattice data obtained at our three lattice spacings to perform the extrapolation to the physical point in the previous section.

VI. PROTON SPIN

In order to extract information on the spin content of the nucleon one needs to evaluate the isoscalar moments A_{20}^{u+d} and B_{20}^{u+d} since the total spin of a quark in the nucleon is given by

$$J^q = \frac{1}{2} (A_{20}^q(0) + B_{20}^q(0)). \quad (23)$$

The total spin can be further decomposed into its orbital angular momentum L^q and its spin component $\Delta\Sigma^q$ as

$$J^q = \frac{1}{2} \Delta\Sigma^q + L^q \quad (24)$$

The spin carried by the u- and d- quarks is determined using $\Delta\Sigma^{u+d} = \tilde{A}_{10}^{u+d}$. In order to evaluate the isoscalar quantities one would need the disconnected contributions. These are notoriously difficult to calculate and they are

neglected in most current evaluations of GFFs. Under the assumption that these are small we may extract the information on the nucleon spin.

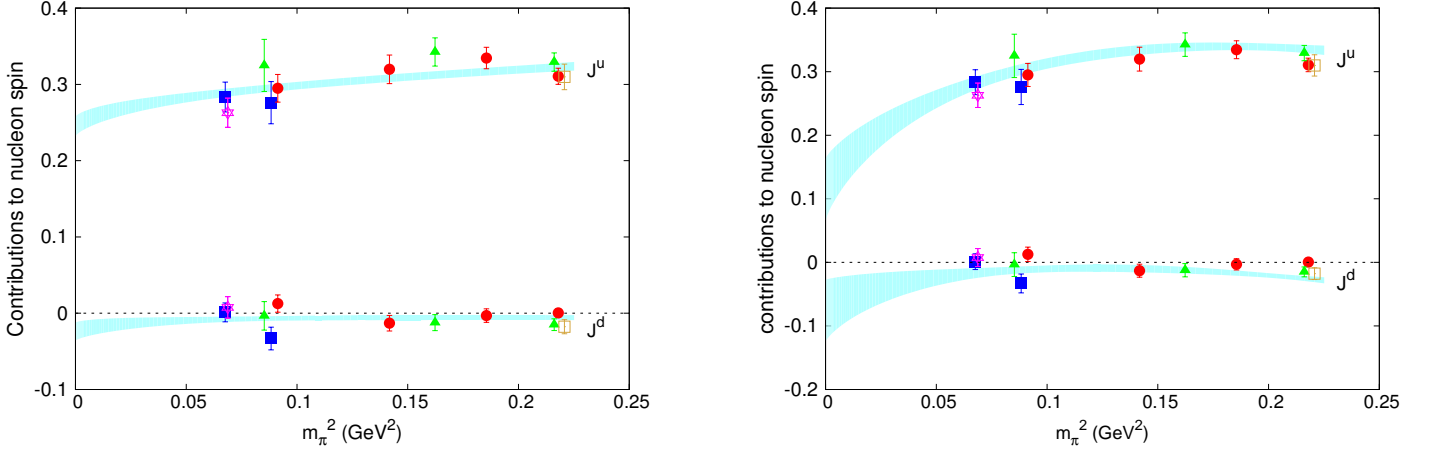


FIG. 14: Chiral extrapolation using $\text{CB}\chi\text{PT}$ (left) and $\text{HB}\chi\text{PT}$ (right) for the total spin carried by the u- and d- quarks.

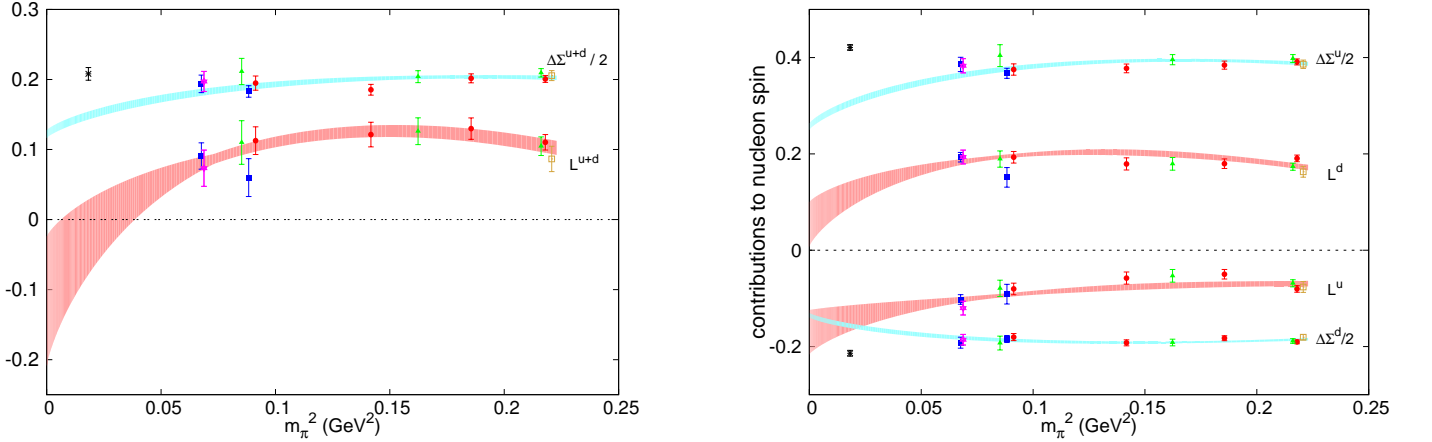


FIG. 15: Chiral extrapolation using $\text{HB}\chi\text{PT}$ for the angular momentum and spin carried by the u- and d- quarks. The physical points, shown by the asterisks are from the HERMES 2007 analysis [52].

In Fig. 11 we show our results for the isoscalar $A_{20}(0)^{u+d}$, $B_{20}(0)^{u+d}$ and $C_{20}(0)^{u+d}$. Since as shown in the previous section, cut-off effects are small, we here perform a chiral extrapolation directly on the lattice data. Having both isoscalar and isovector quantities we can extract the spin J^u and J^d carried by the u- and d- quarks. The results are shown in Fig. 14. We show the extrapolation using both $\text{HB}\chi\text{PT}$ and $\text{CB}\chi\text{PT}$ both of which have the same qualitative behavior. As can be seen, the contribution to the spin from the d-quark is much smaller than that of the u-quarks. These results are in qualitative agreement with the recent results obtained using a hybrid action [42]. In Fig. 15 we show separately the orbital angular momentum and spin carried by the u- and d- quarks. Both our results and those of LHPC [42] are in qualitative agreement as far as the spin is concerned. For the orbital angular momentum we obtain higher values for both d- and u-quark (less negative). Thus we obtain a total positive L^{u+d} compared to a small negative value in the case of LHPC. After chiral extrapolation, the value obtained at the physical point is consistent with zero in agreement with the value determined by LHPC. For the spin contribution $\Delta\Sigma^{u+d}$ our value is lower at the physical point as compared to that obtained by LHPC. We summarize the values for the total spin, orbital angular momentum and spin in the proton at the physical point in Table II.

	CB χ PT	HB χ PT	experiment
J^{u-d}		0.236(14)	
J^{u+d}		0.143(56)	
J^u	0.266(9)	0.189(29)	
J^d	-0.015(8)	-0.047(28)	
$\Delta\Sigma^{u-d}/2$		0.462(11)	
$\Delta\Sigma^{u+d}/2$		0.148(5)	0.208(9)
$\Delta\Sigma^u/2$		0.305(7)	0.421(6)
$\Delta\Sigma^d/2$		-0.157(5)	-0.214(6)
L^{u-d}		-0.258(5)	
L^{u+d}		-0.025(53)	
L^u		-0.141(30)	
L^d		0.116(27)	

TABLE II: Values of nucleon spin observables at the physical point using CB χ PT and HB χ PT and from experiment [52].

VII. CONCLUSIONS

We have performed an analysis on the generalized form factors, $A_{20}(Q^2)$, $B_{20}(Q^2)$, $C_{20}(Q^2)$, $\tilde{A}_{20}(Q^2)$, $\tilde{B}_{20}(Q^2)$, extracted from the nucleon matrix elements of the one-derivative vector and axial-vector operators using two degenerate flavors of twisted mass fermions. Our results are non-perturbatively renormalized and they are presented in the $\overline{\text{MS}}$ scheme at a scale of 2 GeV. To investigate volume and cut-off effects we have used the isovector combinations, which can be calculated without the necessity to evaluate disconnected contributions. Our main conclusion regarding cut-off effects is that they are small within the current accuracy of about 5-10% and for lattice spacings smaller than 0.1 fm. Similarly, no systematic volume effects are seen. Given the small cut-off effects one can compare lattice results directly using different discretization schemes. The comparison of the results using $N_F = 2$ twisted mass fermions with the results obtained using $N_F = 2$ clover fermions by the QCDSF [40] shows agreement. Both the results of this work as well as those by QCDSF are non-perturbatively renormalized. We also compared our results with $N_F = 2 + 1$ domain wall fermions [41]. Again there is agreement without any indication of any systematic effect from including a dynamical strange quark. Our results at three values of the lattice spacing allow for a continuum extrapolation. By interpolating results to a reference mass in units of r_0 and performing a linear extrapolation in a^2 it was shown that the values obtained are consistent with those obtained with a constant extrapolation. This has been verified for both the heaviest and lightest masses used in this work. Furthermore, if one performs chiral fits to the extrapolated continuum results one finds a value at the physical point consistent with the one obtained using directly the lattice data at finite lattice spacing. This provides a consistency check that cut-off effects for a lattice spacing less than 0.1 fm are smaller than our current statistical errors.

Having established that both volume and cut-off effects are small for the isovector quantities for which only connected contributions are needed, we analyse the corresponding isoscalar quantities using directly our lattice data. Of particular interest here is the spin content of the nucleon. The disconnected contributions to the isoscalar quantities are not included. We find that the spin carried by the d-quark is almost zero whereas the u-quarks carry about 50% of the nucleon's spin. This result is consistent with other lattice calculations [42].

For the chiral extrapolations of these quantities we use HB χ PT and CB χ PT theory. In both cases, our results on the momentum fraction and helicity moment at the physical point are higher than their experimental value. Such discrepancies are also observed in the case of the nucleon axial charge and they need to be further investigated.

Acknowledgments

We would like to thank all members of ETMC for a very constructive and enjoyable collaboration and for the many fruitful discussions that took place during the development of this work.

Numerical calculations have used HPC resources from GENCI (IDRIS and CINES) Grant 2009-052271 and CC-IN2P3 as well as from the John von Neumann-Institute for Computing on the Juropa and Jugene systems at the research center in Jülich. We thank the staff members for their kind and sustained support. M.Papinutto acknowledges financial support by the Marie Curie European Reintegration Grant of the 7th European Community Framework

Programme under contract number PERG05-GA-2009-249309. This work is supported in part by the DFG Sonderforschungsbereich/ Transregio SFB/TR9 and by funding received from the Cyprus Research Promotion Foundation under contracts EPYAN/0506/08, KY-Γ/0907/11/ and TECHNOLOGY/ΘΕΠΠΣ/0308(BE)/17.

-
- [1] P. Hagler et al. (LHPC), Phys. Rev. **D77**, 094502 (2008), 0705.4295.
[2] S. N. Syritsyn et al., Phys. Rev. **D81**, 034507 (2010), 0907.4194.
[3] D. Brommel et al. (QCDSF-UKQCD), PoS **LAT2007**, 158 (2007), 0710.1534.
[4] C. Alexandrou, PoS **LATTICE2010**, 001 (2010), 1011.3660.
[5] T. Yamazaki et al., Phys. Rev. **D79**, 114505 (2009), 0904.2039.
[6] C. Alexandrou et al. (ETM Collaboration), Phys.Rev. **D83**, 045010 (2011), 1012.0857.
[7] D. Mueller, D. Robaschik, B. Geyer, F. Dittes, and J. Horejsi, Fortsch.Phys. **42**, 101 (1994), hep-ph/9812448.
[8] X.-D. Ji, Phys.Rev. **D55**, 7114 (1997), hep-ph/9609381.
[9] A. Radyushkin, Phys.Rev. **D56**, 5524 (1997), hep-ph/9704207.
[10] X.-D. Ji, Phys.Rev.Lett. **78**, 610 (1997), hep-ph/9603249.
[11] S. Chekanov et al. (ZEUS Collaboration), JHEP **0905**, 108 (2009), 0812.2517.
[12] F. Aaron et al. (H1 Collaboration), Phys.Lett. **B659**, 796 (2008), 0709.4114.
[13] A. Airapetian et al. (HERMES collaboration), JHEP **0911**, 083 (2009), 0909.3587.
[14] C. Munoz Camacho et al. (Jefferson Lab Hall A Collaboration, Hall A DVCS Collaboration), Phys.Rev.Lett. **97**, 262002 (2006), nucl-ex/0607029.
[15] S. Stepanyan et al. (CLAS Collaboration), Phys.Rev.Lett. **87**, 182002 (2001), hep-ex/0107043.
[16] M. Diehl, Phys. Rept. **388**, 41 (2003), hep-ph/0307382.
[17] C. Alexandrou, M. Brinet, J. Carbonell, M. Constantinou, P. Harraud, et al. (2011), * Temporary entry *, 1102.2208.
[18] R. Frezzotti, P. A. Grassi, S. Sint, and P. Weisz (Alpha), JHEP **0108**, 058 (2001), hep-lat/0101001.
[19] R. Frezzotti and G. C. Rossi, JHEP **08**, 007 (2004), hep-lat/0306014.
[20] P. Weisz, Nucl. Phys. **B212**, 1 (1983).
[21] A. Shindler, Phys. Rept. **461**, 37 (2008), 0707.4093.
[22] C. Alexandrou (2009), 0906.4137.
[23] C. Alexandrou et al. (ETM), Phys. Rev. **D80**, 114503 (2009), 0910.2419.
[24] V. Drach et al., PoS **LATTICE2008**, 123 (2008), 0905.2894.
[25] C. Alexandrou et al. (European Twisted Mass), Phys. Rev. **D78**, 014509 (2008), 0803.3190.
[26] C. Alexandrou et al. (ETM Collaboration), PoS **LAT2007**, 087 (2007), arXiv:0710.1173 [hep-lat].
[27] P. Dimopoulos, R. Frezzotti, C. Michael, G. C. Rossi, and C. Urbach, Phys. Rev. **D81**, 034509 (2010), 0908.0451.
[28] V. Drach et al., PoS **Lattice 2010**, 123 (2010).
[29] C. Alexandrou (ETM Collaboration), PoS **Lattice 2010**, 001 (2010).
[30] C. Alexandrou et al., PoS **LAT2009**, 145 (2009), 0910.3309.
[31] C. Alexandrou et al., PoS **LAT2008 B414**, 145 (2008), hep-lat/9211042.
[32] C. Alexandrou, S. Gusken, F. Jegerlehner, K. Schilling, and R. Sommer, Nucl. Phys. **B414**, 815 (1994), hep-lat/9211042.
[33] S. Gusken, Nucl. Phys. Proc. Suppl. **17**, 361 (1990).
[34] D. Dolgov et al. (LHPC), Phys. Rev. **D66**, 034506 (2002), hep-lat/0201021.
[35] M. Gockeler et al., Phys. Rev. **D54**, 5705 (1996), hep-lat/9602029.
[36] C. Urbach, PoS **LAT2007**, 022 (2007).
[37] C. Alexandrou, M. Constantinou, T. Korzec, H. Panagopoulos, and F. Stylianou, Phys.Rev. **D83**, 014503 (2011), 1006.1920.
[38] M. Gockeler et al., Nucl. Phys. **B544**, 699 (1999), hep-lat/9807044.
[39] M. Constantinou, V. Lubicz, H. Panagopoulos, and F. Stylianou, JHEP **10**, 064 (2009), 0907.0381.
[40] D. Pleiter et al. (QCDSF/UKQCD Collaboration), PoS **LATTICE2010**, 153 (2010), * Temporary entry *, 1101.2326.
[41] Y. Aoki et al., Phys. Rev. **D82**, 014501 (2010), 1003.3387.
[42] J. D. Bratt et al. (LHPC) (2010), 1001.3620.
[43] D. B. Renner, PoS **LAT2009**, 018 (2009), 1002.0925.
[44] S. Alekhin, J. Blumlein, S. Klein, and S. Moch, Phys. Rev. **D81**, 014032 (2010), 0908.2766.
[45] A. Airapetian et al. (HERMES Collaboration), Phys.Lett. **B682**, 345 (2010), 0907.2596.
[46] J. Blumlein and H. Bottcher, Nucl. Phys. **B841**, 205 (2010), 1005.3113.
[47] J. Pumplin, D. Stump, J. Huston, H. Lai, P. M. Nadolsky, et al., JHEP **0207**, 012 (2002), hep-ph/0201195.
[48] A. D. Martin, R. G. Roberts, W. J. Stirling, and R. S. Thorne, Eur. Phys. J. **C28**, 455 (2003), hep-ph/0211080.
[49] D. Arndt and M. J. Savage, Nucl. Phys. **A697**, 429 (2002), nucl-th/0105045.
[50] W. Detmold, W. Melnitchouk, and A. W. Thomas, Phys. Rev. **D66**, 054501 (2002), hep-lat/0206001.
[51] M. Dorati, T. A. Gail, and T. R. Hemmert, Nucl. Phys. **A798**, 96 (2008), nucl-th/0703073.
[52] A. Airapetian et al. (HERMES Collaboration), Phys.Rev. **D75**, 012007 (2007), hep-ex/0609039.
[53] M. Diehl, A. Manashov, and A. Schafer, Eur.Phys.J. **A31**, 335 (2007), hep-ph/0611101.

Appendix A: Expressions for the extraction of GFFs from lattice measurements

We collect here the expressions relating the plateau values to the GFFs A_{20} , B_{20} , C_{20} and \tilde{A}_{20} , \tilde{B}_{20} . The index V (A) refers to the vector (axial-vector) one-derivative operator. All relations are given in Euclidean space.

Vector:

$$\begin{aligned} \Pi_V^{00}(\Gamma^0, \vec{q}) &= A_{20} C \left(-\frac{3E_N}{8} - \frac{E_N^2}{4m_N} - \frac{m_N}{8} \right) + B_{20} C \left(-\frac{E_N}{8} + \frac{E_N^3}{8m_N^2} + \frac{E_N^2}{16m_N} - \frac{m_N}{16} \right) \\ &+ C_{20} C \left(\frac{E_N}{2} - \frac{E_N^3}{2m_N^2} + \frac{E_N^2}{4m_N} - \frac{m_N}{4} \right), \end{aligned} \quad (25)$$

$$\Pi_V^{00}(\Gamma^n, \vec{q}) = 0, \quad (26)$$

$$\begin{aligned} \Pi_V^{kk}(\Gamma^0, \vec{q}) &= A_{20} C \left(\frac{E_N}{8} + \frac{m_N}{8} + \frac{q_k^2}{4m_N} \right) + B_{20} C \left(-\frac{E_N^2}{16m_N} + \frac{m_N}{16} - \frac{q_k^2 E_N}{8m_N^2} + \frac{q_k^2}{8m_N} \right) \\ &+ C_{20} C \left(-\frac{E_N^2}{4m_N} + \frac{m_N}{4} + \frac{q_k^2 E_N}{2m_N^2} + \frac{q_k^2}{2m_N} \right), \end{aligned} \quad (27)$$

$$\Pi_V^{kk}(\Gamma^n, \vec{q}) = A_{20} C \left(i \frac{\epsilon_{kn0\rho} q_k q_\rho}{4m_N} \right) + B_{20} C \left(i \frac{\epsilon_{kn0\rho} q_k q_\rho}{4m_N} \right), \quad (28)$$

$$\Pi_V^{k0}(\Gamma^0, \vec{q}) = A_{20} C \left(-i \frac{q_k}{4} - i \frac{q_k E_N}{4m_N} \right) + B_{20} C \left(-i \frac{q_k}{8} + i \frac{q_k E_N^2}{8m_N^2} \right) + C_{20} C \left(i \frac{q_k}{2} - i \frac{q_k E_N^2}{2m_N^2} \right), \quad (29)$$

$$\Pi_V^{k0}(\Gamma^n, \vec{q}) = A_{20} C \left(\epsilon_{kn0\rho} \left(\frac{q_\rho}{8} + \frac{q_\rho E_N}{8m_N} \right) \right) + B_{20} C \left(\epsilon_{kn0\rho} \left(\frac{q_\rho}{8} + \frac{q_\rho E_N}{8m_N} \right) \right), \quad (30)$$

$$\Pi_V^{kj}(\Gamma^0, \vec{q}) = A_{20} C \frac{q_k q_j}{4m_N} + B_{20} C \left(-\frac{q_k q_j E_N}{8m_N^2} + \frac{q_k q_j}{8m_N} \right) + C_{20} C \left(\frac{q_k q_j E_N}{2m_N^2} + \frac{q_k q_j}{2m_N} \right), \quad (31)$$

$$\Pi_V^{kj}(\Gamma^n, \vec{q}) = A_{20} C \left(i \frac{\epsilon_{kn0\rho} q_j q_\rho}{8m_N} + i \frac{\epsilon_{jn0\rho} q_k q_\rho}{8m_N} \right) + B_{20} C \left(i \frac{\epsilon_{kn0\rho} q_j q_\rho}{8m_N} + i \frac{\epsilon_{jn0\rho} q_k q_\rho}{8m_N} \right). \quad (32)$$

Axial – Vector :

$$\Pi_A^{\mu\nu}(\Gamma^0, \vec{q}) = 0, \quad (34)$$

$$\Pi_A^{k0}(\Gamma^n, \vec{q}) = \tilde{A}_{20} C \left(-i \delta_{nk} \left(\frac{E_N}{4} + \frac{E_N^2}{8m_N} + \frac{m_N}{8} \right) - i \frac{q_k q_n}{8m_N} \right) + \tilde{B}_{20} C \left(i \frac{q_k q_n E_N}{8m_N^2} \right), \quad (35)$$

$$\Pi_A^{kj}(\Gamma^n, \vec{q}) = \tilde{A}_{20} C \left(\delta_{nj} \left(\frac{q_k}{8} + \frac{q_k E_N}{8m_N} \right) + \delta_{nk} \left(\frac{q_j}{8} + \frac{q_j E_N}{8m_N} \right) \right) + \tilde{B}_{20} C \left(-\frac{q_k q_j q_n}{8m_N^2} \right), \quad (36)$$

where $C = \sqrt{2m_N^2/(E_N(E_N + m_N))}$, $E_N^2 = m_N^2 + \vec{q}^2$ and the Latin indices k, j, n denote spatial directions 1, 2, 3 and $k \neq j$. A summation is implied over the index ρ .

Appendix B: Chiral perturbation theory results

For convenience we collect in this appendix the results of HB χ PT results taken from Ref. [53] for the isovector ($I = 1$) and isoscalar ($I = 0$) first moments and axial charge:

$$\begin{aligned}\tilde{A}_{20}^{I=1}(0) &= \tilde{A}_{20}^{I=1(0)} \left\{ 1 - \frac{m_\pi^2}{(4\pi f_\pi)^2} \left[(2g_A^2 + 1) \ln \frac{m_\pi^2}{\lambda^2} + g_A^2 \right] \right\} + \tilde{A}_{20}^{I=1(2,m)} m_\pi^2 \\ \tilde{B}_{20}^{I=1}(0) &= \tilde{B}_{20}^{I=1(0)} \left\{ 1 - \frac{m_\pi^2}{(4\pi f_\pi)^2} \left[(2g_A^2 + 1) \ln \frac{m_\pi^2}{\lambda^2} + g_A^2 \right] \right\} + \tilde{A}_{20}^{I=1(0)} \frac{m_\pi^2 g_A^2}{3(4\pi f_\pi)^2} \ln \frac{m_\pi^2}{\lambda^2} + \tilde{B}_{20}^{I=1(2,m)} m_\pi^2\end{aligned}\quad (37)$$

$$\tilde{A}_{10}^{I=1}(0) = \tilde{A}_{10}^{I=1(0)} \left\{ 1 - \frac{m_\pi^2}{(4\pi f_\pi)^2} \left[(2g_A^2 + 1) \ln \frac{m_\pi^2}{\lambda^2} + g_A^2 \right] \right\} + \tilde{A}_{10}^{I=1(2,m)} m_\pi^2 \quad (38)$$

$$\begin{aligned}A_{20}^{I=1}(0) &= A_{20}^{I=1(0)} \left\{ 1 - \frac{m_\pi^2}{(4\pi f_\pi)^2} \left[(3g_A^2 + 1) \ln \frac{m_\pi^2}{\lambda^2} + 2g_A^2 \right] \right\} + A_{20}^{I=1(2,m)} m_\pi^2 \\ B_{20}^{I=1}(0) &= B_{20}^{I=1(0)} \left\{ 1 - \frac{m_\pi^2}{(4\pi f_\pi)^2} \left[(2g_A^2 + 1) \ln \frac{m_\pi^2}{\lambda^2} + 2g_A^2 \right] \right\} + A_{20}^{I=1(0)} \frac{m_\pi^2 g_A^2}{(4\pi f_\pi)^2} \ln \frac{m_\pi^2}{\lambda^2} + B_{20}^{I=1(2,m)} m_\pi^2\end{aligned}\quad (39)$$

$$\begin{aligned}A_{20}^{I=0}(0) &= A_{20}^{I=0(0)} + A_{20}^{I=0(2,m)} m_\pi^2 \\ B_{20}^{I=0}(0) &= B_{20}^{I=0(0)} \left[1 - \frac{3g_A^2 m_\pi^2}{(4\pi f_\pi)^2} \ln \frac{m_\pi^2}{\lambda^2} \right] - A_{20}^{I=0(0)} \frac{3g_A^2 m_\pi^2}{(4\pi f_\pi)^2} \ln \frac{m_\pi^2}{\lambda^2} + B_{20}^{I=0(2,m)} m_\pi^2 + B_{20}^{I=0(2,\pi)}(0)\end{aligned}\quad (40)$$

$$\tilde{A}_{10}^{I=0}(0) = \tilde{A}_{10}^{I=0(0)} \left\{ 1 - \frac{3g_A^2 m_\pi^2}{(4\pi f_\pi)^2} \left[\ln \frac{m_\pi^2}{\lambda^2} + 1 \right] \right\} + \tilde{A}_{10}^{I=0(2,m)} m_\pi^2 \quad (41)$$

We note that the expressions for $A_{20}^{I=1}$ and $\tilde{A}_{20}^{I=1}$ are the same as those given in Eq. (22) (up to a redefinition of C , \tilde{C} and c_8 , \tilde{c}_8). We have included them here using the notation of Ref. [53] for completeness.

We performed a combined fit to the following CB χ PT results taken from Ref. [51]:

$$\begin{aligned}A_{20}^{I=1}(0) &= a_{20}^v + \frac{a_{20}^v m_\pi^2}{(4\pi f_\pi)^2} \left[-(3g_A^2 + 1) \ln \frac{m_\pi^2}{\lambda^2} - 2g_A^2 + g_A^2 \frac{m_\pi^2}{M_0^2} \left(1 + 3 \ln \frac{m_\pi^2}{M_0^2} \right) \right. \\ &\quad \left. - \frac{1}{2} g_A^2 \frac{m_\pi^4}{M_0^4} \ln \frac{m_\pi^2}{M_0^2} + g_A^2 \frac{m_\pi}{\sqrt{4M_0^2 - m_\pi^2}} \left(14 - 8 \frac{m_\pi^2}{M_0^2} + \frac{m_\pi^4}{M_0^4} \right) \arccos \left(\frac{m_\pi}{2M_0} \right) \right] \\ &\quad + \frac{\Delta a_{20}^v(0) g_A m_\pi^2}{3(4\pi f_\pi)^2} \left[2 \frac{m_\pi^2}{M_0^2} \left(1 + 3 \ln \frac{m_\pi^2}{M_0^2} \right) - \frac{m_\pi^4}{M_0^4} \ln \frac{m_\pi^2}{M_0^2} + \frac{2m_\pi(4M_0^2 - m_\pi^2)^{\frac{3}{2}}}{M_0^4} \arccos \left(\frac{m_\pi}{2M_0} \right) \right] \\ &\quad + 4m_\pi^2 \frac{c_8^{(\lambda)}}{M_0^2} + \mathcal{O}(p^3)\end{aligned}\quad (42)$$

$$\begin{aligned}B_{20}^{I=1}(0) &= b_{20}^v \frac{M_N(m_\pi)}{M_0} + \frac{a_{20}^v g_A^2 m_\pi^2}{(4\pi f_\pi)^2} \left[\left(3 + \ln \frac{m_\pi^2}{M_0^2} \right) - \frac{m_\pi^2}{M_0^2} \left(2 + 3 \ln \frac{m_\pi^2}{M_0^2} \right) \right. \\ &\quad \left. + \frac{m_\pi^4}{M_0^4} \ln \frac{m_\pi^2}{M_0^2} - \frac{2m_\pi}{\sqrt{4M_0^2 - m_\pi^2}} \left(5 - 5 \frac{m_\pi^2}{M_0^2} + \frac{m_\pi^4}{M_0^4} \right) \arccos \left(\frac{m_\pi}{2M_0} \right) \right] + \mathcal{O}(p^3)\end{aligned}\quad (43)$$

$$\begin{aligned}C_{20}^{I=1}(0) &= c_{20}^v \frac{M_N(m_\pi)}{M_0} + \frac{a_{20}^v g_A^2 m_\pi^2}{12(4\pi f_\pi)^2} \left[-1 + 2 \frac{m_\pi^2}{M_0^2} \left(1 + \ln \frac{m_\pi^2}{M_0^2} \right) \right. \\ &\quad \left. - \frac{m_\pi^4}{M_0^4} \ln \frac{m_\pi^2}{M_0^2} + \frac{2m_\pi}{\sqrt{4M_0^2 - m_\pi^2}} \left(2 - 4 \frac{m_\pi^2}{M_0^2} + \frac{m_\pi^4}{M_0^4} \right) \arccos \left(\frac{m_\pi}{2M_0} \right) \right] + \mathcal{O}(p^3)\end{aligned}\quad (44)$$

$$\begin{aligned}
A_{20}^{I=0}(0) &= a_{20}^s + 4m_\pi^2 \frac{c_9}{M_0^2} - \frac{3a_{20}^s g_A^2 m_\pi^2}{(4\pi f_\pi)^2} \left[\frac{m_\pi^2}{M_0^2} + \frac{m_\pi^2}{M_0^2} \left(2 - \frac{m_\pi^2}{M_0^2} \right) \ln \frac{m_\pi}{M_0} \right. \\
&\quad \left. + \frac{m_\pi}{\sqrt{4M_0^2 - m_\pi^2}} \left(2 - 4\frac{m_\pi^2}{M_0^2} + \frac{m_\pi^4}{M_0^4} \right) \arccos \left(\frac{m_\pi}{2M_0} \right) \right] + \mathcal{O}(p^3)
\end{aligned} \tag{45}$$

$$\begin{aligned}
B_{20}^{I=0}(0) &= b_{20}^s \frac{M_N(m_\pi)}{M_0} - \frac{3a_{20}^s g_A^2 m_\pi^2}{(4\pi f_\pi)^2} \left[\left(3 + \ln \frac{m_\pi}{M_0} \right) - \frac{m_\pi^2}{M_0^2} \left(2 + 3 \ln \frac{m_\pi}{M_0} \right) \right. \\
&\quad \left. + \frac{m_\pi^4}{M_0^4} \ln \frac{m_\pi}{M_0} - \frac{2m_\pi}{\sqrt{4M_0^2 - m_\pi^2}} \left(5 - 5\frac{m_\pi^2}{M_0^2} + \frac{m_\pi^4}{M_0^4} \right) \arccos \left(\frac{m_\pi}{2M_0} \right) \right] + \mathcal{O}(p^3)
\end{aligned} \tag{46}$$

$$\begin{aligned}
C_{20}^{I=0}(0) &= c_{20}^s \frac{M_N(m_\pi)}{M_0} - \frac{a_{20}^s g_A^2 m_\pi^2}{4(4\pi f_\pi)^2} \left[-1 + 2\frac{m_\pi^2}{M_0^2} \left(1 + \ln \frac{m_\pi}{M_0} \right) \right. \\
&\quad \left. - \frac{m_\pi^4}{M_0^4} \ln \frac{m_\pi}{M_0} + \frac{2m_\pi}{\sqrt{4M_0^2 - m_\pi^2}} \left(2 - 4\frac{m_\pi^2}{M_0^2} + \frac{m_\pi^4}{M_0^4} \right) \arccos \left(\frac{m_\pi}{2M_0} \right) \right] + \mathcal{O}(p^3)
\end{aligned} \tag{47}$$

where M_0 is the mass of the nucleon at the chiral limit.

Appendix C: Numerical results for the isovector sector

m_π (GeV) (no. confs)	$(Q)^2$	A_{20}	B_{20}	\tilde{A}_{20}	\tilde{B}_{20}
$\beta = 3.9, 24^3 \times 48$					
0.4675 (477)	0.0	0.256(9)	0.364(23)	0.307(6)	0.651(99)
	0.322	0.230(7)	0.337(18)	0.273(5)	0.487(121)
	0.619(1)	0.202(9)	0.299(16)	0.252(7)	0.568(72)
	0.897(2)	0.178(12)	0.277(22)	0.227(11)	0.456(69)
	1.157(3)	0.172(19)	0.249(34)	0.176(17)	0.078(96)
	1.404(4)	0.154(22)	0.232(34)	0.191(22)	0.319(65)
	1.640(6)	0.136(40)	0.208(60)	0.193(51)	0.346(126)
0.4319 (365)	0.0	0.257(10)	0.418(34)	0.310(7)	0.516(109)
	0.321	0.219(8)	0.361(29)	0.264(7)	0.431(155)
	0.615(1)	0.185(9)	0.296(26)	0.232(9)	0.378(75)
	0.888(3)	0.167(13)	0.257(34)	0.211(14)	0.339(86)
	1.143(4)	0.168(26)	0.209(42)	0.175(25)	0.191(115)
	1.385(6)	0.141(29)	0.151(42)	0.173(37)	0.242(99)
	1.614(8)	0.103(48)	0.118(63)	0.136(67)	0.139(112)
0.3770 (553)	0.0	0.258(10)	0.408(44)	0.296(8)	0.683(150)
	0.320	0.217(10)	0.360(32)	0.266(7)	0.878(170)
	0.613(1)	0.192(11)	0.338(26)	0.253(8)	0.417(89)
	0.884(3)	0.164(20)	0.265(40)	0.237(26)	0.349(132)
	1.138(4)	0.204(76)	0.339(129)	0.288(91)	0.661(301)
	1.377(6)	0.166(59)	0.271(97)	0.218(70)	0.402(176)
	1.604(8)	0.105(92)	0.140(126)	0.143(113)	0.215(210)
0.3032 (943)	0.0	0.255(16)	0.309(40)	0.284(10)	0.277(136)
	0.317(1)	0.239(13)	0.241(36)	0.268(10)	0.380(184)
	0.601(2)	0.199(13)	0.268(32)	0.223(11)	0.048(104)
	0.862(4)	0.174(23)	0.178(37)	0.195(20)	0.245(110)
	1.103(6)	0.135(27)	0.156(45)	0.172(24)	0.304(118)
	1.330(8)	0.098(21)	0.142(34)	0.135(22)	0.180(70)
	1.543(10)	0.105(34)	0.097(40)	0.087(27)	0.051(75)

TABLE III: Results on A_{20} and B_{20} form factors at $\beta = 3.9$, lattice size: $24^3 \times 48$

m_π (GeV) (no. confs)	$(Q)^2$	A_{20}	B_{20}	\tilde{A}_{20}	\tilde{B}_{20}
$\beta = 3.9, 32^3 \times 64$					
0.2978 (351)	0.0	0.243(15)	0.375(67)	0.287(10)	0.413(95)
	0.183	0.230(14)	0.382(67)	0.262(8)	0.454(215)
	0.354(1)	0.207(14)	0.318(54)	0.244(7)	0.282(98)
	0.516(1)	0.196(14)	0.298(50)	0.228(9)	0.298(100)
	0.670(2)	0.164(20)	0.249(61)	0.228(15)	0.441(138)
	0.817(3)	0.165(16)	0.206(44)	0.204(11)	0.318(65)
	0.957(4)	0.154(18)	0.188(40)	0.179(14)	0.165(64)
	1.222(6)	0.145(28)	0.173(55)	0.191(38)	0.252(110)
1.348(7)	0.095(23)	0.170(42)	0.151(36)	0.123(81)	
0.2600 (667)	0.0	0.263(13)	0.301(47)	0.275(13)	0.752(174)
	0.182	0.240(09)	0.284(52)	0.261(10)	0.666(331)
	0.352(1)	0.222(10)	0.252(38)	0.259(11)	0.582(164)
	0.512(1)	0.196(12)	0.221(40)	0.256(16)	0.524(158)
	0.664(2)	0.185(17)	0.246(48)	0.216(19)	0.263(185)
	0.808(3)	0.161(14)	0.233(34)	0.217(16)	0.378(105)
	0.945(4)	0.143(15)	0.204(34)	0.181(18)	0.247(93)
	1.205(6)	0.100(22)	0.122(42)	0.127(24)	0.140(128)
1.328(7)	0.106(22)	0.162(40)	0.124(26)	0.072(105)	

TABLE IV: Results on A_{20} and B_{20} form factors at $\beta = 3.9$, lattice size: $32^3 \times 64$

m_π (GeV) (no. confs)	$(Q)^2$	A_{20}	B_{20}	\tilde{A}_{20}	\tilde{B}_{20}
$\beta = 4.05, 32^3 \times 64$					
0.4653 (419)	0.0	0.258(9)	0.431(26)	0.303(7)	0.579(92)
	0.294	0.231(7)	0.382(22)	0.270(6)	0.458(166)
	0.568(1)	0.210(7)	0.329(20)	0.248(7)	0.523(73)
	0.824(2)	0.197(12)	0.283(25)	0.232(11)	0.342(77)
	1.067(3)	0.170(19)	0.313(41)	0.221(20)	0.263(116)
	1.297(4)	0.166(19)	0.256(30)	0.211(21)	0.367(75)
	1.517(5)	0.156(31)	0.208(43)	0.181(33)	0.256(76)
	1.930(7)	0.084(29)	0.085(34)	0.111(30)	0.190(92)
2.126(9)	0.056(58)	0.054(63)	0.066(65)	0.114(139)	
0.4032 (326)	0.0	0.244(12)	0.465(46)	0.312(10)	0.625(114)
	0.293	0.240(10)	0.434(42)	0.287(10)	0.455(206)
	0.564(1)	0.208(11)	0.356(36)	0.263(11)	0.477(91)
	0.816(2)	0.197(17)	0.302(43)	0.259(19)	0.539(132)
	1.053(3)	0.175(32)	0.225(48)	0.251(34)	0.307(154)
	1.278(5)	0.144(20)	0.203(36)	0.195(22)	0.332(81)
	1.493(6)	0.144(41)	0.204(66)	0.202(56)	0.387(137)
	1.895(9)	0.068(25)	0.095(36)	0.093(26)	0.142(73)
2.084(10)	0.043(26)	0.083(45)	0.071(32)	0.151(76)	
0.2925 (447)	0.0(0)	0.231(24)	0.426(67)	0.310(23)	0.283(268)
	0.291(1)	0.237(20)	0.307(66)	0.279(15)	0.328(322)
	0.556(2)	0.216(21)	0.343(47)	0.252(18)	0.459(202)
	0.801(3)	0.236(41)	0.279(69)	0.223(33)	0.025(207)
	1.029(5)	0.136(39)	0.116(77)	0.165(34)	0.028(238)
	1.245(7)	0.139(72)	0.090(84)	0.219(95)	0.484(266)
	1.450(10)	0.104(42)	0.132(67)	0.157(52)	0.273(129)

TABLE V: Results on A_{20} and B_{20} form factors at $\beta = 4.05$

m_π (GeV) (no. confs)	$(Q)^2$	A_{20}	B_{20}	\tilde{A}_{20}	\tilde{B}_{20}
$\beta = 4.2, 32^3 \times 64$					
0.4698 (357)	0.0	0.252(13)	0.402(35)	0.295(9)	0.768(126)
	0.467(1)	0.215(12)	0.343(29)	0.272(8)	0.606(145)
	0.886(2)	0.205(14)	0.264(29)	0.260(11)	0.595(95)
	1.270(4)	0.214(27)	0.220(47)	0.249(27)	0.523(141)
	1.627(6)	0.140(37)	0.240(78)	0.178(47)	0.030(159)
	1.961(8)	0.131(36)	0.127(40)	0.177(39)	0.226(113)
	2.276(10)	0.118(29)	0.057(25)	0.114(28)	0.146(83)
	2.861(14)	0.056(40)	0.017(43)	0.054(28)	0.058(100)
$\beta = 4.2, 48^3 \times 96$					
0.2622 (245)	0.0	0.276(21)	0.234(45)	0.290(15)	0.579(129)
	0.211	0.255(14)	0.264(49)	0.275(12)	0.301(375)
	0.407(2)	0.253(16)	0.205(38)	0.279(11)	0.689(146)
	0.589(3)	0.228(17)	0.157(45)	0.255(12)	0.268(137)
	0.762(5)	0.184(30)	0.180(59)	0.272(27)	0.453(213)
	0.925(7)	0.193(23)	0.178(38)	0.231(15)	0.177(107)
	1.081(9)	0.174(22)	0.146(39)	0.230(17)	0.207(100)
	1.373(13)	0.133(39)	0.076(49)	0.167(23)	0.168(114)
	1.511(16)	0.093(28)	0.142(40)	0.164(20)	0.189(82)
	1.644(18)	0.054(38)	0.153(52)	0.118(29)	-0.001(95)
	1.773(20)	0.026(37)	0.138(62)	0.152(40)	0.031(107)

TABLE VI: Results on A_{20} and B_{20} form factors at $\beta = 4.2$